



Characterization of laser cladding functional coatings: an in-situ monitoring and variability analysis approach

Malek Mousa¹ · Hany Osman¹ · Ahmed Azab¹ · Abdalnasser El-Gaddar¹ · Fazle Baki²

Received: 7 August 2023 / Accepted: 8 May 2024 / Published online: 28 May 2024
© The Author(s), under exclusive licence to Springer-Verlag London Ltd., part of Springer Nature 2024

Abstract

In this industry 4.0 era, additive manufacturing is proving to be a key manufacturing technology with great potential. Laser additive manufacturing-directed energy deposition, the directed energy deposition variant that utilizes metal powder, is ideal for metallic part repair and coating. It is also referred to as powder-blown laser cladding. Relatively, it is a newer additive technology that is currently attracting a lot of research. This paper uses in-situ monitoring and statistical analysis to characterize the multi-track height powder-blown laser cladding functional coating. This study investigates the effect of laser scanning speed, laser power, and shield gas flow rates on the melt pool temperature and image area. Multi-track functional coating samples are built of one layer under different shield gas flow rates and laser scanning speed levels. The powder flow rate is kept constant at its ideal level (16.2 g/min). The sensor signals, alternatively called process signatures, such as melt pool temperature and melt pool image, are gathered and used in the conducted statistical analysis to predict the process response. Multi-track height is measured after sectioning the samples. Most related work focuses on the three major process parameters: laser power, laser beam scanning speed, and powder feeding rate. A dearth of the literature considers shield gas flow rate even though it is proving significant, especially in cases with a sudden geometry change. Even though there is a shortage in functional coating (multi-track cladding) characterization, non-commercial-like scenarios such as single bead (single track) are well studied by other researchers. In-situ monitoring of the process and incorporation of sensor signals are hardly addressed for multi-track cladding. The analysis conducted in this research revealed that the shield gas flow rate, laser scanning speed, and their interaction significantly affect the functional coating's multi-track height, melt pool image area, and melt pool temperature. Moreover, a separate experiment has been conducted to identify how the laser scanning speed and laser power affect the heating adequacy and how that relates, in turn, to the quality of the multi-track coating produced. This study paves the way for the integration of in-situ monitoring, which is rarely used in standardized commercial systems, exploring the use of process signatures in predicting the process response.

Keywords Laser additive manufacturing directed energy deposition · Functional coating · Shield gas flow rate · Laser scanning speed · Laser power · Process signatures · Multi-track height

1 Introduction and background

Laser additive manufacturing directed energy deposition (LAM-DED) enables building and repairing shapes that are not achievable by conventional manufacturing. It allows for

gradual material composition, complex shapes, and undercuts. Also, LAM-DED is employed in anti-wear surface treatments because of its small heat-affected zone, lower dilution rate, and decent metallurgical bonding between coating and substrate.

There is a lack of accurate analytical models of the laser cladding process since it involves complex physical phenomena and intricate interacting process parameters. Building a suitable multi-physics model for real-time control and decision-making is challenging. Multi-physics models involve physical phenomena such as heat transfer, fluid flow, surface tension, free surface movement, and material phase change [1]. Thus, researchers have struggled to develop accurate

✉ Ahmed Azab
azab@uwindsor.ca

¹ Production & Operations Management Research Lab,
Faculty of Engineering, University of Windsor, 401 Sunset
St, Windsor, ON N9B 3P4, Canada

² Odette School of Business, University of Windsor, Windsor,
ON, Canada

analytical, closed-form models and simulations for this complex deposition process [2]. As a result, experimental data analysis rather than complex multi-physical ones becomes desired.

On the experimental side, there are challenges in generalizing the outcomes of such experimental work in laser cladding characterization due to the process complexity and the narrow process parameter windows; slight variations in the process parameters and conditions can significantly affect the quality of the product [1]. Characterization studies that address various process parameters are essential to increase the knowledge of the laser cladding process and the interactions between the different process parameters, signatures, and response. A few studies exist on the characterization of laser cladding. Although the shield gas flow rate (SGFR) can be significant, especially in cases with a sudden geometry change [3], SGFR is hardly addressed in the literature [4]. This shortage of literature might be attributed to early research conducted on process gases on flat surfaces, which concludes that the impact of process gases is negligible [5]. A plethora of literature addresses simple structures such as single-track and thin walls [4]. However, the functional coating of multi-track cladding used for many commercial applications is rarely explored. To the best of the authors' knowledge, the effect of varying SGFR and its interaction with laser scanning speed (LSS) has not been investigated in previous studies that utilize in-situ monitoring in multi-track laser cladding.

This article aims to contribute to the body of knowledge of LAM-DED by exploring the effect of SGFR and LSS as well as their interaction on the process build quality, including multi-track height (MTH), and process signatures, including melt pool image area (MPIA) and melt pool temperature (MPT). Additionally, the relationship between the laser power (LP) and LSS has been investigated. Interesting findings have been arrived at regarding the correlation and contribution of the two factors to the melting pool's heating level. These findings also further investigate how this, in turn, impacts the quality of the multi-track coating. In-situ process monitoring is utilized to gather the process signatures: MPT and melt pool images (MPI). Image processing is done for the taken melt pool imagery. MPIA is used as a process signature for multi-track functional coating characterization for the first time in the literature. The relationships between the process parameters and process signatures and that between the process parameters and MTH are identified through the variability analysis and data visualization developed and proposed in Section 3. It is worth mentioning that the MTH is tackled in this article due to its direct effect on the coating's functional properties, such as wear resistance.

1.1 LAM-DED laser beam and nozzle configurations

Nasiri and Khosravani [6] illustrate the design of the deposition head. Such a head, which consists of a laser beam guiding and focusing optics and a metal powder delivery nozzle, has the most significant influence on the printing process. They listed four categories of deposition head designs, which are annular laser beam base nozzles (Fig. 1a), lateral nozzle or off-axis nozzle (Fig. 1b), discrete coaxial nozzle (Fig. 1c), and continuous coaxial nozzles (Fig. 1d). In annular laser beam base nozzles, the powder is injected from the center of the nozzle, and the laser radiates coaxially in a cone around the powder stream (Fig. 1a). This type of nozzle is utilized in research. However, its unique design makes it challenging to manufacture [7]. The lateral nozzle uses a single nozzle that injects powder into the melt pool created by the laser (Fig. 1b). Its simple geometry and low cost make it suitable for forward processes such as fast coating and rotatory parts. However, the tool path dependency limits its application in manufacturing complicated geometries. The discrete coaxial nozzle has more than one powder injector (at least three injectors) located around the nozzle's axis. At the same time, the laser beam emits from the center (Fig. 1c). In these nozzles, the powder is injected from several directions, which enables it to clad in every direction. Furthermore, when the cladding head is tilted, the gravity force does not affect the powder distribution at the outlet. This ability makes the nozzle suitable for mounting on a five-axis driver in complicated geometries (3D printing) manufacturing. However, compared to continuous coaxial nozzles, the discrete nozzle has lower catchment efficiency and reduced clad quality in practice [7]. In continuous coaxial nozzles, the powder flow coming from the powder feeder is divided into three (or more) equal flows and sent to a ring-shaped expansion chamber on the top part of the nozzle. A homogeneous powder cloud forms in the chamber and enters a cone-shaped gap. Therefore, the powder will leave the nozzle in the form of a hollow cone (Fig. 1d). The main advantage of this type of nozzle is the high homogeneity of the powder flow profile at the outlet, leading to high efficiency and quality of cladding. However, tilting the nozzle is somewhat limited because gravity strongly affects the distribution of the powder inside the expansion chamber, which in turn influences the homogeneity of the powder at the outlet.

1.2 Process monitoring

This subsection explores the related work about mapping factors through process monitoring. In LAM-DED, the

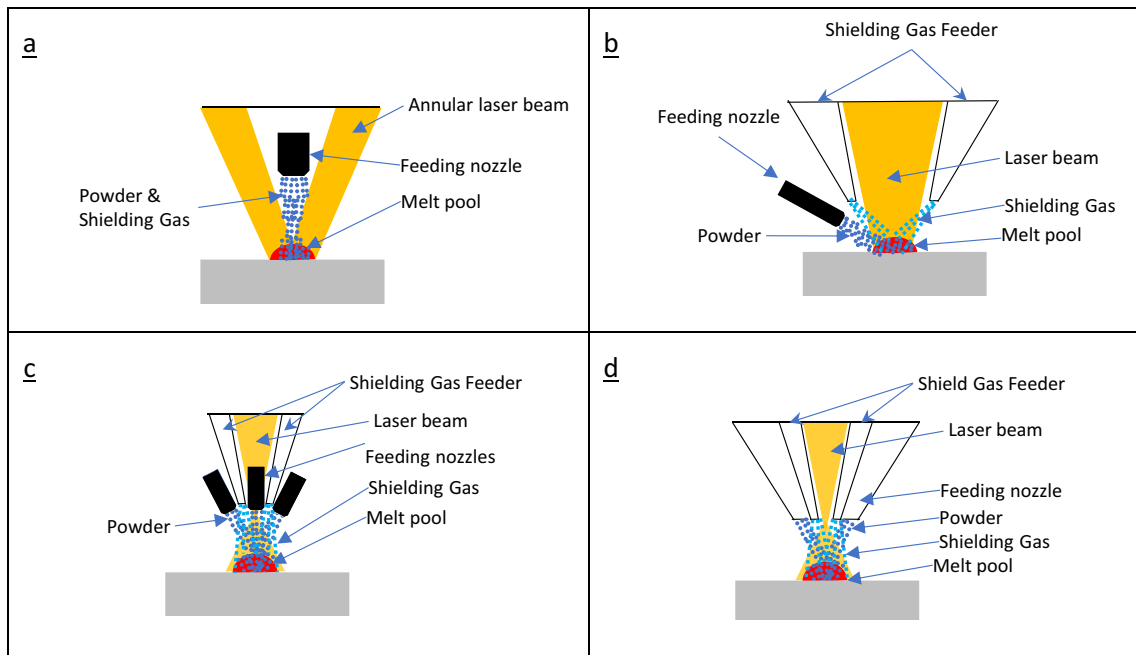


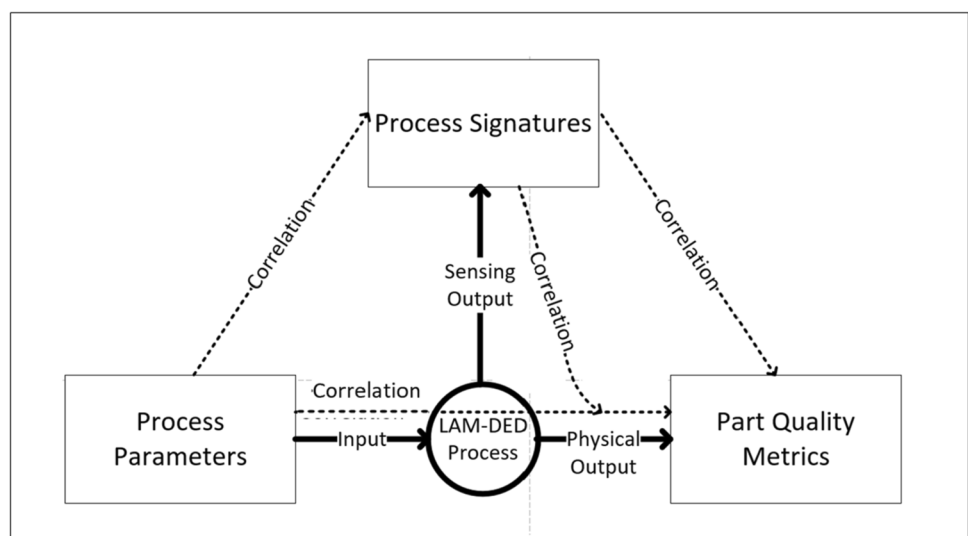
Fig. 1 Four types of deposition configuration LAM-DED: **a** annular laser beam base nozzle, **b** lateral (off-axis feeding) nozzle, **c** discrete coaxial nozzle, and **d** continuous coaxial nozzle. Adapted from Nasiri and Khosravani [6]

ultimate objective for the operator is to obtain a high-quality and repeatable process. The critical purpose of the monitoring systems is to map the relationship between process parameters and process response to indicate the process state and, hence, the predicted part quality [8]. This article uses in-situ monitoring to gather data, i.e., process signatures, mainly MPI and MPT. MTH, MPT, and MPIA characterizations become achievable with appropriate monitoring and data analysis. Figure 2 shows the possible mappings between process parameters, process signatures, and part quality. In the LAM-DED process, the

parameters are the process inputs. Process signatures are the process outputs measured by various sensory devices, and the part quality metric for the functionally coated part is the MTH. As shown in Fig. 2, there is a correlation between the process parameters and both the process signatures and the part quality. There is also a correlation between the process signature and the part quality, as well as that between the combination of process signatures and process parameters and the part quality [9].

Haley et al. [10] reviewed the in-situ process monitoring for hybrid DED. The review reported extensive research on

Fig. 2 Mapping process parameters to process signature and part quality (based on the figure in Spears and Gold [9])



in-situ inspection methods to gain insights into and regulate the melt pool dynamics in additive manufacturing. These methods can be off axis or on axis to the energy source and can measure different signals such as imaging, thermography, spectroscopy, or topography. Vision signals are the most widely used method to extract the geometrical features of the melt pool and surface defects. High-speed imaging can identify the geometric information of the melt pool and even the particle interaction behavior with the melt pool surface [10]. Melt pool images are typically captured with low spatial and spectral resolution sensors, which can detect irregularities in DED structures [11]. Digital image processing can precisely extract the melt pool geometry, which helps to regulate machine parameters [12] and identify microstructure defects [13]. The accuracy of vision sensing is highly dependent on camera resolution, which necessitates the acquisition and processing of large datasets over a long time. Analyzing the data with machine learning allows for controlling melt pool dynamics and identifying defects [10].

Table 1 outlines the features of commercialized LAM-DED processes. The LENS process involves using a gantry-type deposition head along with a fiber laser. Optomec's 850R LENS has a melt pool sensor with a vision camera that can provide feedback control. Optomec Inc. has developed a LENS modular print engine that integrates the deposition head into a conventional CNC machine tool. The DM3D's M1 Metal AM WAAM System uses three types of lasers and has two types of deposition heads: the gantry and the robot arm. Inssteck's MX-Fab DMT process uses a fiber laser and a gantry-type deposition head and employs two vision cameras for closed-loop control of the layer thickness. Trumpf Inc. has developed the TruLaser Cell Series (7040), which includes three types of lasers and a gantry-type deposition head. Trumpf Inc.'s LMD process uses a vision camera to monitor the formation of the molten pool during the deposition process. DMG Mori LASERTEC 6000 DED HYBRID incorporates a thermal imaging camera that enables observation across the entire operational space, facilitates adaptive process control, and ensures continuous monitoring of the working distance. It also includes a powder feed rate sensor

for precise measurement and automatic powder calibration. An AM evaluator is integrated to visualize pertinent process data, such as melt pool size and powder mass flow, in a digital 3D model and in a chronological sequence.

Yet monitoring is still not utilized in all the standardized DED and LENS systems currently available on the market. Users of the DED technology should be building generic DED systems that utilize in-situ monitoring, capitalizing on the advances in digital cameras and robotic systems. The melt pool's monitoring data provide insights, which could possibly enable operators to make informed decisions, leading to improved overall performance and outcomes in the production of built components, especially in cases where it is augmented with real-time monitoring and control of the system.

1.3 Process parameters in LAM-DED

LAM-DED is known to be affected by significant parameters, such as laser power, laser speed, and laser powder flow rate. Laser power and powder flow rate have been studied by researchers such as Yuan et al. [15], Xi et al. [16], and Sampson et al. [17]. Multi-track (functional coating) is little studied, and SGFR as a parameter is not considered in characterization studies for multi-track characterization.

The effect of LSS on MPT while fixing other parameters is studied by Farshidianfar [18]. Many other researchers, such as Xi et al. [16] and Sampson et al. [17], investigate the LSS combined with powder flow rate and laser power or combined with laser power alone [19]. As a unique importance, LSS affects the energy absorbed and the accumulation of powder that builds the melt pool on the top of the substrate (Ye et al. [4]). LSS interacts with laser power and powder feed rate. For this reason, LSS is selected as a variable in this study.

Many previous studies do not focus on investigating the effects of SGFR. Koruba et al. [5] stated that the impact of process gases is usually overlooked in experimental studies because some early research on performing laser cladding on flat surfaces concludes that the SGFR can be considered

Table 1 Available commercial LENS and DED systems with monitoring systems, adapted from [14]

Process	Company	Model	Type of nozzle	Monitoring of molten pool
LENS	Optomec	Optomec 850R	Coaxial	One melt pool sensor vision camera
WAAM	DM3D	M1 Metal AM System	Coaxial	Two high-speed cameras
DED	Inssteck	MX-Fab	Coaxial	Two high-def camera
Includes DED	Trumpf	TruLaser Cell Series (7040)	Coaxial	One vision camera
DED	DMG Mori	LASERTEC 6000 DED HYBRID	Coaxial	One thermal imaging camera

DED processes include laser engineering net shaping (LENS). WAAM refers to wire arc additive manufacturing

negligible. Nonetheless, the SGFR can become significant in sudden geometric changes, such as steps, edges, and fillet geometry features [3].

Along with LSS and SGFR that are investigated to evaluate their effect on MTH, MPT, and MPIA, the rest of the process parameters such as laser power, powder flow rate, laser spot size, the powder material and size, substrate material, the distance between the nozzle and the substrate, and the carrier gas flow rate (CGFR) are kept unchanged in this study.

1.4 Influence of parameters on process signatures and quality

A plethora of literature has examined the relationships between process parameters, signatures, and quality. Process parameters can significantly impact the cladding build and the process signatures [20].

Table 2, adapted from a recent literature review by Ye et al. [4], enumerates the different process parameters,

process signatures, and part quality factors. The shield gas flow sub-factor “rate” is marked in black, indicating a shortage in research related to SGFR. This paper addresses the influences of the level of power, LSS, and SGFR and their combined impact on the MTH, MPIA, and MPT. A three-factor ANOVA experiment is conducted to examine the impacts of these factors, and conclusions are made using hypothesis testing.

Table 3 summarizes the effect of LSS and SGFR on MTH and MPIA. There is a shortage of research on in-situ monitoring in multi-track laser LAM-DED. To the authors’ knowledge, the melt pool image area (MPIA), along with melt pool image properties, has not been studied in research related to multi-track LAM-DED characterization. The MTH of the functional coating is reasonably addressed in previous research, as the MTH can be measured offline after the cladding is completed. The effect of SGFR on the single track height can vary based on other interacting parameters, such as carrying gas flow rate (CGFR), laser power (LP), PFR, and LSS, as reported by Sommer et al. [21] shown on

Table 2 A summary of the factors and metrics in LAM-DED clustered as process parameters, signatures, or part quality. Adapted from Ye et al. [4]. Process parameter “shield gas flow rate” is in scope

Process parameter	Process signature			Part quality
	Melt pool	Track	Layer	
Laser beam	Temperature	Geometry	Geometry	Physical
- Power ^{a, b}	- Peak ^{a, b}	- Width ^b	- Irregularity ^a	- Roughness ^a
- Scanning speed ^{a, b}	- Gradient ^{a, b}	- Height ^{a, b}	Microstructure ^a	- Residual stress ^a
- Diameter ^{a, b}	Geometry	- Shrinkage	Defects	- Appearance ^a
- Distribuon	- Width ^{a, b}	- Irregularity ^a	- Porosity	- Melng state ^{a, b}
- Scanning mode ^{a, b}	- Length ^{a, b}	Microstructure ^b	- Lack of fusion	- Porosity ^{a, b}
- Hatch spacing ^a	- Depth ^{a, b}	- Crystal structure	- Cracks	- Cracks ^b
- Power density ^{a, b}	- Area ^{a, b}	- Metal phase	- Contaminaon	- Overheang ^a
Shielding gas flow ^a	- Contour ^b	Defects	Average roughness ^a	Geometric
- Rate	Emission	- Porosity ^a	Residual stress	- Form and size ^b
- Pattern	- Opca ^{a, b}	- Lack of fusion ^a		- Shrinkage ^a
Powder	- Acousc ^{a, b}	Diluon ^b		Mechanical
- Feeding rate ^b	Plume ^{a, b}	Cooling rate ^{a, b}		- Strength ^{a, b}
- Powder size ^a	Spaera			- Hardness ^b
- Layer thickness ^a				- Toughness
- Absorpvity ^b				- Wear rate ^b
- Reflectance				
Substrate ^b				

Table 3 Summary of literature that includes the effect of SGFR and LSS on MTH and MPIA

Authors/year	Clad material	Configuration			Operation range	SGFR range LSS range	Input		Height	MPIA
		Single track	Multi-track	3D structure			SGFR	LSS		
Sommer et al. [21]	AISI 316L	X			LP (W): 1350 LBD (mm): 1.2 LSS (mm/s): 90 PFR (g/min): 15 CGFR (l/m): 5–10 SGFR (l/min): 5–20	SGFR (l/min): 5 to <20 CGFR (l/m): =5–6 l/m SGFR (l/min): 20 CGFR (l/m): 5 to 6	↑	–	–	
Kattire et al. [22]	CPM 9 V steel	X			LP (W): 1700–2700 LBD (mm): 3 LSS (mm/s): 3.3–13.3 PFR (g/min): 5–15 SGFR (l/min): 15–25	SGFR (l/min): 15–25	↑	–	–	
Koruba et al. [5]	Stellite 6 (cobalt based alloy)		X		LP (W): 400 LBD (mm): 1.5 LSS (mm/s): PFR (g/min): 1.8 CGFR (l/m): 4–10 SGFR (l/m): 10–15	SGFR (l/min): 10–15 CGFR (l/m): 4 and 10	↑	–	↓	
Eo et al. [23]	316L		X		SGFR (l/min): 5–25 LP (W): 3500–2900 LBS (mm × mm): 12 × 4 LSS (mm/s): 4, 10	SGFR (l/min): 15 to 25	↑	–	↓	
Kattire et al. [22]	CPM 9 V steel	X			LP (W): 1700–2700 LBD (mm): 3 LSS (mm/s): 3.3–13.3 PFR (g/min): 5–15 SGFR (l/min): 15–25	LSS (mm/s): 3.3–13.3	–	↑	↓	
Kummailil et al. [24]	Ti–6Al–4 V		X		LP (W): 250–350 PFR (g/min): 2.28–4.4 LSS (mm/s): 16.9–27.5	LSS (mm/s): 16.9–27.5	–	↑	↓	
Arthur et al. [25]	Ti–6Al–4 V			X	LP (W): 320–400 LBD (mm): 1 LSS (mm/s): 6.35–10.58 PFR (g/min): 1.42–1.49	LSS (mm/s): 6.35–10.58	–	↑	↓	
Srisingsitthisunti et al. [26]	Inconel 625	X			LP (W): 500–1000 LSS (mm/s): 3.6 PFR (g/min): 15 SGFR (l/min): 15	LSS (mm/s): 3.6 SGFR (l/min): 15	–	↑	↓	

LP, laser power; LBD, laser beam diameter; PFR, powder flow rate; LSS, laser scanning speed; SGFR, shield gas flow rate; CGFR, carrier gas flow rate

the first row of Table 3. While keeping the LSS constant at a considerably large LSS (90 m/s) on a thin substrate, single-track cladding, with large particles (50–150 μm) increasing the SGFR to 20 l/min, shows a sudden increase in single-track height value [21]. The cause of the sudden increase in single-track height might be that the carrier gas and the shield gas help deliver the powder into the melt pool bath [22]. On the other hand, both Sommer et al. [21] and Kattire et al. [22] report that the SGFR effect can be negligible on the single-track height at levels that do not include interaction between the SGFR and CGFR. A larger SGFR can blow away the powder and cause the height value to drop [5]. Eo et al. [23] conduct a laser cladding study with 316 L HIS stainless steel varying the argon SGFR level in the range of 5–25 l/min, with different levels of LSS and LP. They

report that the oxygen content is decreased with an increase in SGFR irrespective of the other process parameters' levels (Eo et al. [23]). Variations in SGFR can change the oxygen content and shape of the melt pool. They also observe that increasing the SGFR from 15 to 25 l/min results in greater weld penetration into the substrate.

Also, Table 3 shows that increasing LSS while maintaining the SGFR constant reduces MTH. Kattire et al. [22] obtained this result by studying the single-track laser cladding, Kummailil et al. [24] studied the multi-track coating, and Arthur et al. [25] studied 3D structures. Furthermore, the MPIA of single track is also reduced with increasing the LSS [26].

The list in Table 4 summarizes the effect of LSS and SGFR on the MPT. No impact is reported on the MPT

Table 4 Literature summary that includes the effect of SGFR and LSS on melt pool temperature (MPT)

Authors/year	Clad material	Configuration			Operation range	SGFR range LSS range	Input		MPT
		Single track	Multi-track	3D structure			SGFR	LSS	
Hua et al. [27]	Rene88DT super-alloy and Ni20 hot spraying alloy			X	LP (W): 1700–2700 LBD (mm): 3 LSS (mm/s): 3.3–13.3 PFR (g/min): 5–15 SGFR (l/min): 15–25	LSS (mm/s): 5 SGFR (l/min): 5–20	↑	–	–
Srisungsitthisunti et al. [26]	Inconel 625	X			LP (W): 400 LBD (mm): 1.5 LSS (mm/s): PFR (g/min): 1.8 CGFR (l/m): 4–10 SGFR (l/m): 10–15	LSS (mm/s): 3,6 SGFR (l/min): 15	–	↑	↓
Hua et al. [27]	Rene88DT super-alloy and Ni20 hot spraying alloy			X	SGFR (l/min): 5–25 LP (W): 3500–2900 LBS (mm × mm): 12 × 4 LSS (mm/s): 4, 10	LSS (mm/s): 5–9–15 SGFR (l/min): 5–20	–	↑	↓
Kledwig et al. [28]	X2CrN-iMo17-12-2	X			LP (W): 1700–2700 LBD (mm): 3 LSS (mm/s): 3.3–13.3 PFR (g/min): 5–15 SGFR (l/min): 15–25 LP (W): 320–400 LBD (mm): 1 LSS (mm/s): 6.35–10.58 PFR (g/min): 1.42–1.49	LSS (mm/s): 13.3–16.7 LSS (mm/s): 20–26.7	–	↑	↓

LP, laser power; LBD, laser beam diameter; PFR, powder flow rate; LSS, laser scanning speed; SGFR, shield gas flow rate; CGFR, carrier gas flow rate

when increasing the SGFR while keeping the LSS constant [27]. Eo et al. [23] found that the temperature of the melt pool greatly influenced the oxidation kinetics.

When LSS is gradually increased to 13.3, 20, and 26.7, MPT experienced an increase, decrease, and no change, respectively [28]. Less absorption time of the laser energy expected at higher LSS leads to reduced MPT. Less powder deposition is also expected when increasing the LSS. Nonetheless, the decrease in absorbed energy and deposited powder varies for each LSS level. If the deposited powder amount is reduced significantly, the MPT may increase. If the absorbed energy is reduced considerably, the MPT may decrease. And if there is a balance in the change between the absorbed power and the deposited powder, no effect of LSS would be noticed.

According to the literature, a range of parameters and their interactions influence the melt-pool temperature, area, and height. Thus, this article considers a significant range of changes in the process parameters: LSS and SGFR, which is not fully captured in similar studies. LSS varies between 10 and 15 m/s; similarly, SGFR is between 9.4 and 28.3 l/min.

Extremely low and high MPTs can indicate insufficient heating and overheating, respectively. Improper selection of LP and LSS can lead to overheating and lack of fusion defects. Overheating can result from excessive LP, slow LSS, or both, which causes lengthy exposure to the laser beam and yields excessive heat input. Conversely, insufficient LP, high LSS, or both cause a lack of fusion because of brief exposure to the laser beam, yielding a lack of heat input for proper fusion. Overheating is not desired as it causes cracks and bubbles in the functional coating. On the other hand, insufficient heating reduces the strength of the functional coating and leads to defects such as a lack of fusion [29]. The feasible cladding melt pool temperature could range from 1200 to 2000 °C, depending on the material and heat transfer to the substrate [30]. For the setup used in this study, good-quality cladding was made while the MPT was within 1650 °C to 1850 °C. In this article, the good-quality zone is called the feasible cladding zone. On the other hand, cladding under MPTs that are higher than 1850 °C and less than 1650 °C are referred to as the overheating zone and the insufficient heat zone, respectively. Sections 3.1 and 3.4 address the heating zones in the conducted characterization study. Section 3.7 looks into the adequacy of heating the melting pool and what that entails in terms of the quality of the produced specimen. The effect of LP, along with LSS, on the MPT, MPIA, and MTH is presented. The rest of the article is structured as follows: Section 2 describes the methodology, Section 3 describes the results and discussion in detail, and finally, Section 4 summarizes the conclusions and future work.

2 Methodology

This section describes the methodology followed in the study. The experiment setup is introduced in Section 3.1. The different factors and outcomes of this study are outlined in Section 3.2. Lastly, data visualization, descriptive statistics, data preparation and filtering, and inferential statistics are presented in Sects. 3.3–3.6.

2.1 Experimental setup

All experiments have been carried out at Lincoln Laser Solutions. The cladding process is carried out using a five-axis CNC equipped with a 4-kW diode (4 mm spot diameter) cladding head and a powder feeder with a continuous coaxial nozzle. The powder flow rate was kept constant (16.2 g/min). The coaxial optical system focuses the laser beam onto the substrate (Fig. 3). The monitoring system that gathers digital MPI and MPT data uses a Pixel link D721MU CMOS camera and a pyrometer is a Lascon LPC04, that is a high-speed fiber-coupled infrared ratio pyrometer, which collects both the MPI and MPT measurements. The distance between the nozzle and the substrate is 17 mm. The substrate size is 2'' × 4'', made of cold rolled structural steel, and the powder material is 316 L HIS, with particle size between 53 and 150 μm. The shield gas is 100% argon gas, with a variable flow rate between 20 CFH (9.44 l/min) and 60 CFH (28.32 l/min).

Two series of experiments are conducted: (1) characterization of MTH, MPIA, and MPT of multi-track laser cladding under SGFR and LSS and their interaction, in which only the medium level of LP is applied: 1575 W; (2) demonstration of heating zone heating effects (e.g., insufficient/adequate/over-heating) on MTH, MPIA, and MPT of multi-track laser cladding, in which only extreme levels (low and high SGFR and LSS) are applied.

Figure 3 shows the levels of the two independent variables: LSS and SGFR, along with a schematic showing the MTH in relation to the multi-track functional coated part. The deposition strategy is based on cladding parallel tracks, which always start at the same edge of the substrate and finish at the other edge of the substrate. In this research, cladding tracks (beads) are deposited right next to each other, in which the deposition nozzle is shifted 2 mm between two successive tracks, resulting in an overlap ratio of 50% [31], which the industry partner recommends reducing the waviness when used with 316 L HIS powder of 53–150 μm particle size.

Figure 4 details different aspects of the conducted experiments: handling of the physical specimens, the flow of data, and the algorithms processed. The Data

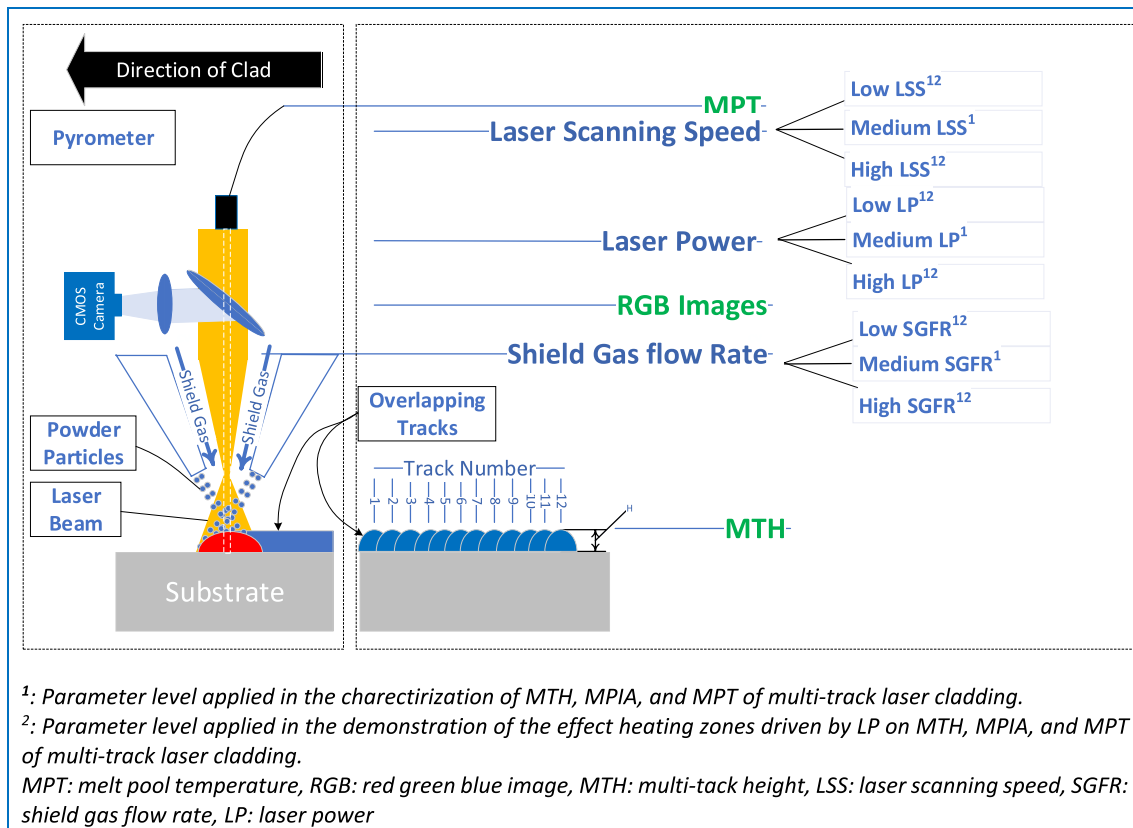


Fig. 3 The front view is a schematic of the process setup; the side view shows the process parameters and dependent variables

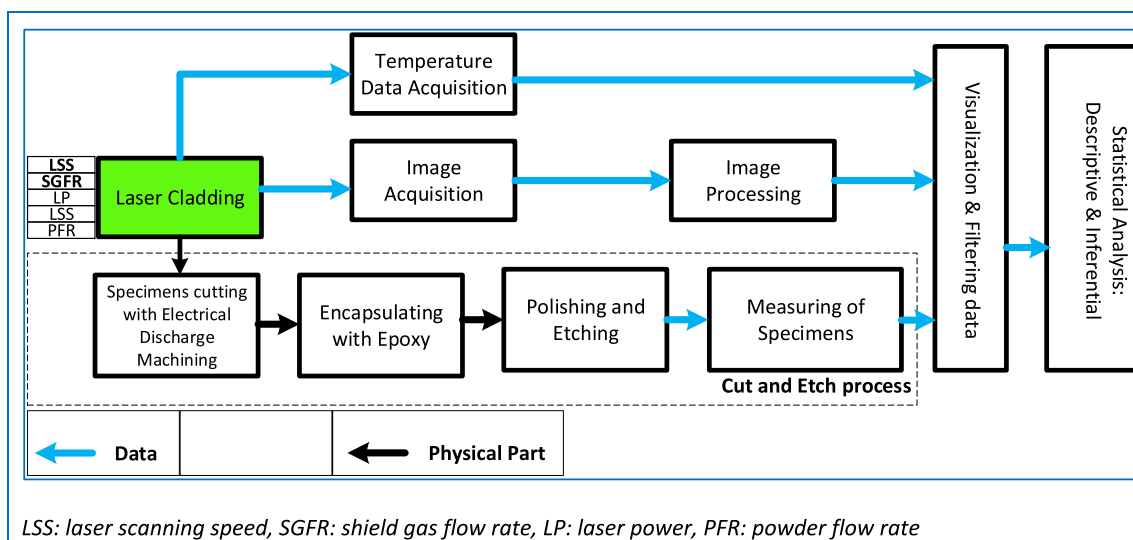


Fig. 4 Schematic detailing the experiments’ handling of the physical specimens, the flow of data, and the algorithms processed

Acquisition System (DAQ) gathers MPT data and MPI during the LAM-DED process. The digital camera images are then analyzed with customized image processing software to compute the MPIA. The data for the MPT and

MPIA are then visualized and filtered to remove outliers. Similarly, the cut and etch process data that include MTH are also visualized and filtered. The last stage of this research consists of the statistical analysis, including

descriptive and inferential statistics, as well as the characterization of the multi-track laser cladding based on the LSS and SGFR.

2.2 Factors and metrics in the study

The dataset collected in this study is decomposed into four types: variable process parameters, predefined process parameters (constants), process signatures, and process outcomes. This section is dedicated to detailing these four different types of data and outcomes.

2.2.1 Process parameters

As explained in Section 2, an extensive list of parameters interacts while depositing the laser clads. Hence, one might be tempted to conduct experiments considering all the possible treatments (combination of factors) to represent the whole population. Such an exhaustive study, though, is impractical due to the impending cost and time limitations on the number of treatments applied. Laser power and powder flow rates are well studied in the literature, as detailed in Section 2. LSS has been also addressed in past literature, such as the single-track research by Kattire et al. [22] and the 3D structure research by Arthur et al. [25]. However, it is essential to note that LSS affects the energy absorbed and the powder deposition that builds the melt pool on the top of the substrate. Thus, LSS interacts with laser power and powder feed rate. For this reason, LSS is selected as a variable process parameter in this study.

There is a shortage of studies in the literature detailing the effects of SGFR. The impact of process gases is overlooked in experimental studies. When performing laser cladding on flat surfaces, researchers conclude that the impact of process gases can be considered negligible [5]. Nonetheless, SGFR is deemed significant when the functional coating is applied to geometry characterized by sudden geometric changes (e.g., steps, edges, fillets) [3]. Accordingly, this article addresses the effect of SGFR on MPIA, MPT, and MTH.

2.2.2 Process signatures

Data measured by sensors during the monitoring process is termed process signatures by the literature [9]. This study collects two process signatures during the monitoring stage:

MPT, which is acquired using a pyrometer, and MPIs, which are taken via a CMOS camera at a rate of 20 frames per second. TIFF and PNG files are relevant choices for displaying complex images, as they hold more information. The PNG format is chosen because they are smaller in size.

Unlike the MPT data, MPI needs further evaluation and image processing. The extensive size of the collected data makes it essential to create a data repository. MATLAB Image Processing Toolbox is used to extract the image features, including MPIA [32]. Because the image data is ideally used in real-time monitoring and control, selecting an image processing program that can agilely analyze the image is essential. This study prioritized image processing accuracy since the MPIA data gathered with in-situ monitoring is analyzed offline. Rapid application development tools are used at this stage of research. Improving the speed of the image processing process is carried out at a later stage, though, where deployment development tools and compilers are utilized, that is beyond the scope of this article. In the worst-case scenario, the maximum elapsed time (duration from start to end of image processing run) is less than 0.2 s when only a PC processor, not a GPU, is utilized. The measurements are taken using the TIC-TOC Stopwatch function in MATLAB on an Intel(R) Core(TM) i7-3770 processor, the clock speed of which is 3.40 GHz, and the L2 cache memory of which is 1.0 MB. The block diagram, shown in Fig. 5, illustrates the stages of image processing. After the digital image data is imported, the image is converted to a gray scale; then, segmentation is used to convert the image to binary classes (black and white) based on a chosen threshold. The threshold is carefully chosen to categorize the melt pool itself, and the noise caused by the light reflection and bright powder particles are yet to join the melt pool. Then, filtering is applied to remove noise shown as small areas in the image categorized as black or white but residing inside relatively bigger areas (connected components) of the opposite binary class. Lastly, the “regionprops” function measures properties, such as area, centroid, and major and minor axes, for each connected component in an image. This article uses the MPIA that is extracted from the image processing program.

Figure 6 shows an example run obtained via the image processing toolbox function: *regionprops* [32]. The label “Area” in the figure represents the number of pixels forming the binary image of the melt pool after applying the

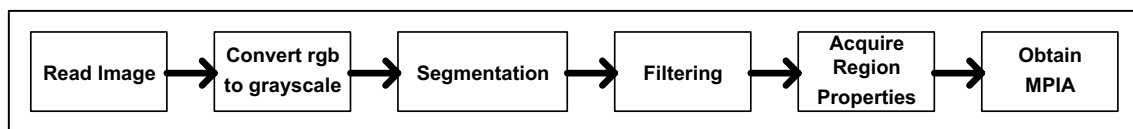


Fig. 5 Block diagram showing the image processing approach carried out to obtain the MPIA

ImageCentroid:	[134.4048 120.9154]
ImageArea:	4360
ImageMajorAxisLength:	79.4913
ImageMinorAxisLength:	69.9120
ImageOrientation:	-89.2196
ImagePerimeter:	232.250
ImageET:	0.1172

Fig. 6 An example of the image processing outcome in which region properties are listed

upstream functions. The label “Centroid” is the X and Y coordinates of the centroid of the melt pool image. Finally, the labels “MajorAxisLength” and “MinorAxisLength” are the lengths (in pixels) of the major and minor axes of the fitted ellipses around the melt pool image regions, respectively.

2.2.3 Process outcomes

This research focuses on the geometry of laser cladding beads. The customer normally specifies the MTH of the laser cladding functional coating. MTH’s dimension is a critical characteristic because it affects the coated component’s fit into the other components of the assembly and influences functional properties such as wear resistance. The cut-polish-etch-inspect process is applied to measure the MTH. This process includes sectioning the laser cladding samples using electrical discharge machining, primary polishing, chemical etching, and finally, an inspection of the specimens under the microscope. This process is followed by an advanced stage, in which the specimens are encapsulated with epoxy material, further polished with fine polishing paper, and then etched with chemical material to prepare them for inspection under the microscope. Figure 7 demonstrates a few of the stages of the cut-polish-etch-inspect process.

2.3 Visualization and descriptive statistics

MTH, MPIA, and MPT data are plotted for the treatment groups categorized using different values for SGFR and LSS. Figure 8 shows the raw data of MPIA and MPT vs. MPIA. Data associated with each group is clustered based on the built conditions: LSS and SGFR levels. It is noticed that different clusters are spread into relatively large ranges of MPT, MPIA, and MTH. These large ranges are driven due to the various melt pool interactions that would not be realized with an experimental study. A simple mean (or median in case of non-parametric statistical analysis) will not reveal the actual effect of parameters on the MP, MPIA, and MTH. Thus, instead of handling the whole group data, the individual means of the 12 tracks are visualized and compared in Sects. 3.1 to 3.7.

2.4 Data preparation

The preparation of raw data aims to make it suitable for further processing and analysis. After the data is collected, it is labeled, visualized, and later cleaned (filtered). MPIA and MPIT data are filtered to remove the outliers. For each group, MPIA data beyond the interquartile range (a measure covered by the middle 50% of the data spanning the second and third quartiles) is removed. Because the rate at which the data is collected (20 frames/s) is constant irrespective of LSS, groups with fast LSS have fewer observations than those with higher LSS.

Since it is inappropriate to carry out the analyses with imbalanced data, each group’s data is adjusted to an equal number of data points to achieve a balanced sample size. It is worth mentioning that the filtered data set has its observations aligned based on distance rather than time to reflect the same progress in cladding for each group regardless of the cladding speed. Table 5 outlines the experiment design for the characterization of MTH, MPIA, and MPT of multi-track laser cladding under SGFR and LSS and their interaction. Only the medium level of LP is applied (1575 W). On the other hand, Table 6 outlines the experiment design for the

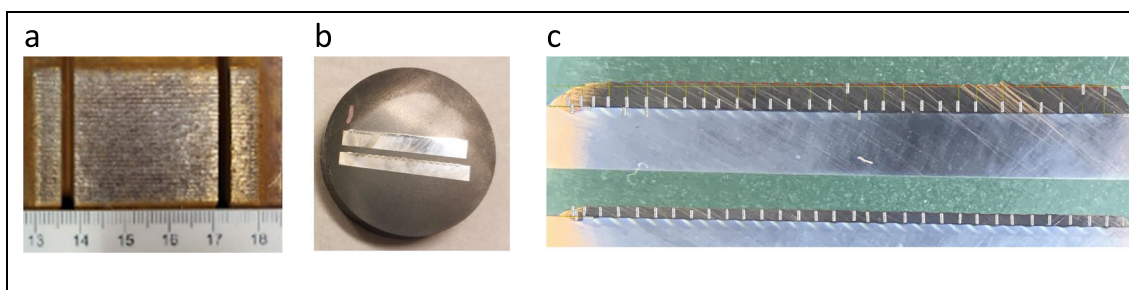


Fig. 7 **a** Multi-track sample; **b** cut polished and etched specimens; **c** magnified image **b**

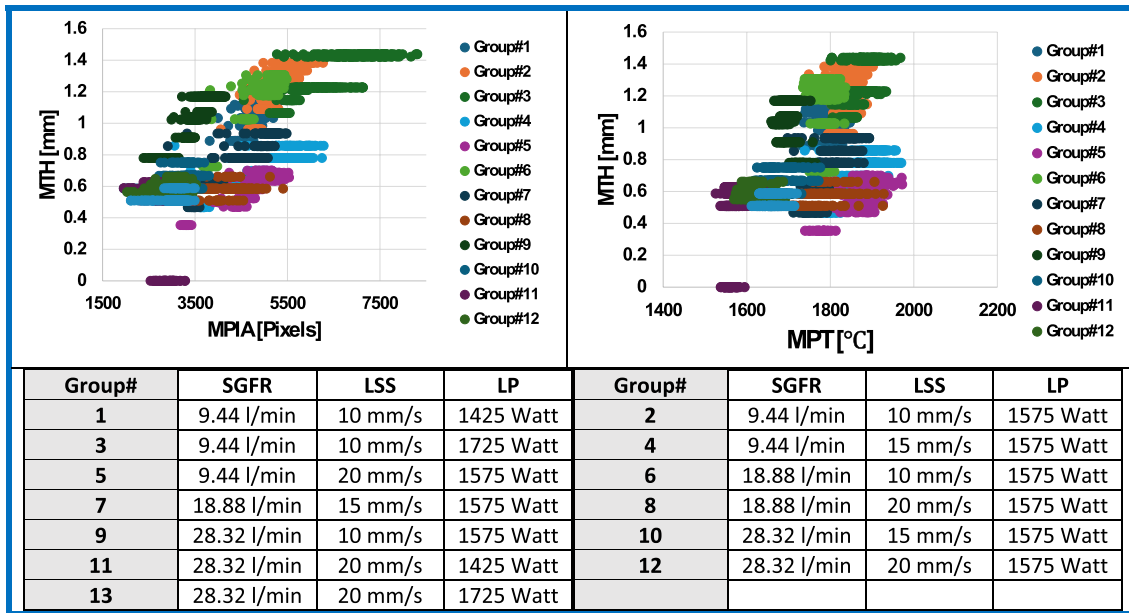


Fig. 8 Clusters plot MPT vs. MPIA

Table 5 Experiment design for the characterization of MTH, MPIA, and MPT of multi-track laser cladding under SGFR and LSS and their interaction. Medium level of LP is applied for all data points in the Table (1575 W)

DOE	Factor A: SGFR		
3 × 3			
Factor B: LSS	Low SGFR (9.44 l/min)	Ideal SGFR (18.88 l/min)	High SGFR (28.32 l/min)
Slow LSS (10 mm/s)	Group# 2	Group# 6	Group# 9
Ideal LSS (15 mm/s)	Group# 4	Group# 7	Group# 10
Fast LSS (20 mm/s)	Group# 5	Group# 8	Group# 12

demonstration of the effect of heating zones driven by laser power and laser scanning speed on MTH, MPIA, and MPT of multi-track laser cladding. In the demonstration of the effect of the heating zones' experiment, only extreme levels (low and high SGFR and LSS) are applied.

2.5 Descriptive statistics

This descriptive statistics section consists of measures of central tendency, variability, and frequency distribution for the MPT, MPIA, and MTH datasets. The datasets are divided into six groups based on the various outlined LSS and SGFR levels. The data studied in this descriptive statistics section is treated and filtered as explained in Section 3.4.

Table 6 Experiment design for the demonstration of the effect of the heating zones driven by LP and LSS on MTH, MPIA, and MPT of multi-track laser cladding. Only the extreme levels (low and high SGFR and LSS) are applied

LSS [mm/s]	LP [W]	SGFR [l/min]	Group
10	1425	9.44	Group #1
10	1575	9.44	Group #2
10	1725	9.44	Group #3
20	1425	28.32	Group #11
20	1575	28.32	Group #12
20	1725	28.32	Group #13

2.5.1 Central tendency and distribution

Table 7 includes the central tendency summary and the standard deviation after filtering the data and removing the outliers. The total number of observations in each group is 1106, which is equal for all the groups. The results and the comparison between groups are discussed in reference to the outlined findings in the literature discussed in Section 2 and in accordance with the physics of the process and are given in Section 4.

2.5.2 Distribution

As normality is one of the assumptions of the two-way ANOVA, the evaluation of normality is essential. This study uses the Shapiro–Wilk test [34] to evaluate the normality of the MPT, MPIA, and MTH data. The null hypothesis for a Shapiro–Wilk test boils down to having

Table 7 Statistics summary of temperature (MPT), area (MPIA), and multi-track height (MTH) [33]

Dependent variable	Group#	SGFR l/min	LSS mm/s	LP Watt	Mode	Median	Mean	Std. deviation	P-value of Shapiro–Wilk	Levene’s test
MPT [°C]	1	9.44	10	1425	1797	1797	1795	22.9	<0.001	F = 93.379 p-value < 0.001
	2	9.44	10	1575	1840	1827	1827	22.2	<0.001	
	3	9.44	10	1725	1849	1869	1871	31.6	0.014	
	4	9.44	15	1575	1907	1890	1879	43.9	<0.001	
	5	9.44	20	1575	1902	1886	1876	46.3	<0.001	
	6	18.88	10	1575	1777	1789	1788	17.4	0.004	
	7	18.88	15	1575	1820	1817	1809	38.6	<0.001	
	8	18.88	20	1575	1814	1789	1785	50.4	0.214	
	9	28.32	10	1575	1688	1699	1700	17.1	<0.001	
	10	28.32	15	1575	1656	1667	1672	30.1	<0.001	
	11	28.32	20	1425	1556	1563	1566	15.9	<0.001	
	12	28.32	20	1575	1601	1606	1610	22.2	<0.001	
	13	28.32	20	1725	1653	1660	1661	21.7	0.279	
MPIA [pixel]	1	9.44	10	1425	4880	4894	4777	377.2	<0.001	F = 106.744 p-value < 0.001
	2	9.44	10	1575	5308	5235	5154	479.2	<0.001	
	3	9.44	10	1725	5727	6062	6164	855.2	<0.001	
	4	9.44	15	1575	4484	5372	5174	650.4	<0.001	
	5	9.44	20	1575	4902	4811	4667	567.3	<0.001	
	6	18.88	10	1575	5134	5070	4941	405.1	<0.001	
	7	18.88	15	1575	4928	4848	4666	555.4	<0.001	
	8	18.88	20	1575	3400	4154	4063	529.9	<0.001	
	9	28.32	10	1575	3673	3705	3634	343.3	<0.001	
	10	28.32	15	1575	3339	3350	3277	322.8	<0.001	
	11	28.32	20	1425	1961	2914	2874	257.4	<0.001	
	12	28.32	20	1575	2965	3052	2999	263.2	<0.001	
	13	28.32	20	1725	3080	3105	3061	245.3	<0.001	
MTH [mm]	1	9.44	10	1425	1.03	1.11	1.05	0.141	<0.001	F = 85.565 p-value < 0.001
	2	9.44	10	1575	1.23	1.22	1.16	0.202	<0.001	
	3	9.44	10	1725	1.23	1.23	1.23	0.213	<0.001	
	4	9.44	15	1575	0.78	0.78	0.74	0.104	<0.001	
	5	9.44	20	1575	0.35	0.64	0.59	0.101	<0.001	
	6	18.88	10	1575	1.03	1.21	1.17	0.149	<0.001	
	7	18.88	15	1575	0.78	0.78	0.81	0.136	<0.001	
	8	18.88	20	1575	0.59	0.59	0.57	0.042	<0.001	
	9	28.32	10	1575	1.17	1.17	1.09	0.122	<0.001	
	10	28.32	15	1575	0.67	0.67	0.66	0.057	<0.001	
	11	28.32	20	1425	0.51	0.59	0.57	0.053	<0.001	
	12	28.32	20	1575	0.55	0.58	0.59	0.035	<0.001	
	13	28.32	20	1725	0.51	0.51	0.53	0.034	<0.001	

the data follow a normal distribution. Thus, conversely, the alternative hypothesis is that the data does not follow a normal distribution. If the *p*-value of the test is less than 0.05, then the null hypothesis is rejected, and there is evidence that the data tested are not normally distributed at a 5% significance level [34]. Table 7 includes the *p*-values of the Shapiro–Wilk test [34] for normality. It is obvious

that the *p*-values of the Shapiro–Wilk’s test are less than 0.5, and thus, it can be concluded that all groups are not normally distributed. A second condition to apply two-way ANOVA is that of homogeneity of variance. The following subsection describes the analysis that has been carried out for the purpose.

2.5.3 Variability

In this subsection, the homogeneity of variance in the MPT, MPIA, and MTH data is evaluated. Both box plots and Levene's test [35] are utilized in the analysis. Box plots for MPT, MPIA, and MTH are included in Figs. 9, 10, and 11. It is evident from the figures that not all the box plots are similar to one another variance-wise. MPT variability (Fig. 9) is the largest in group 1. Groups 6 and 9 show the least variability. MPIA variabilities (Fig. 10) reach their maximum in groups 7 and 9. MTH variabilities of groups 1 and 7, as demonstrated in Fig. 11, are much higher than those in other groups. It is worth noting that some outliers represent natural variations in the population; they have been kept in the dataset, as the box plots show (Figs. 9, 10, and 11).

Along with box blots, Levene's tests [35] are conducted to evaluate the homogeneity of variance, which is one of the conditions for carrying out the two-way ANOVA analysis as outlined earlier in Section 3.5.2. The null hypothesis for Levene's test is that the population variances are equal. If the resulting p -value in Levene's test is less than the critical value ($\alpha=0.05$), the groups are deemed not to have equal variances. Levene's test p -values are included in Table 7. The p -value for Levene's test is less than 0.05 for MPT, which signifies at least one group with a variance that differs significantly from the other groups. The same conclusion can be found by looking at Levene's test results for MPIA and MTH, as the p -values in the two cases are less than 0.05.

Fig. 9 Box plot of MPT data

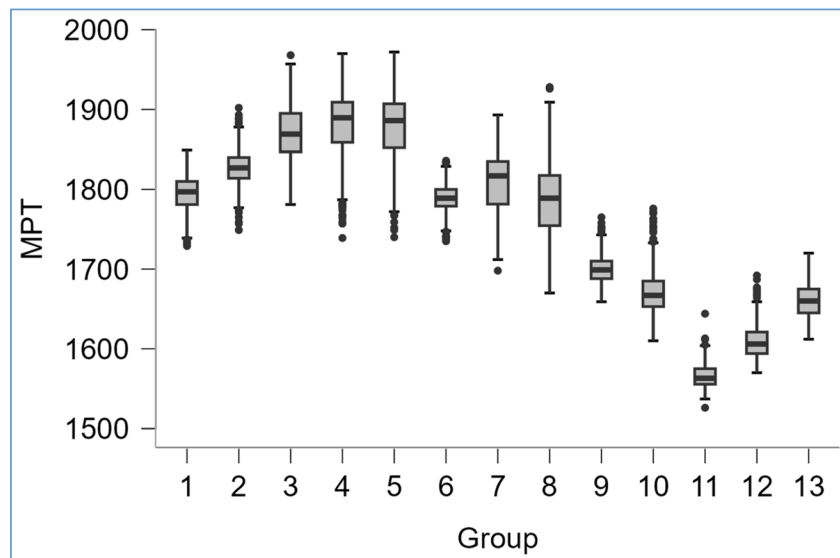


Fig. 10 Box plot of MPIA data

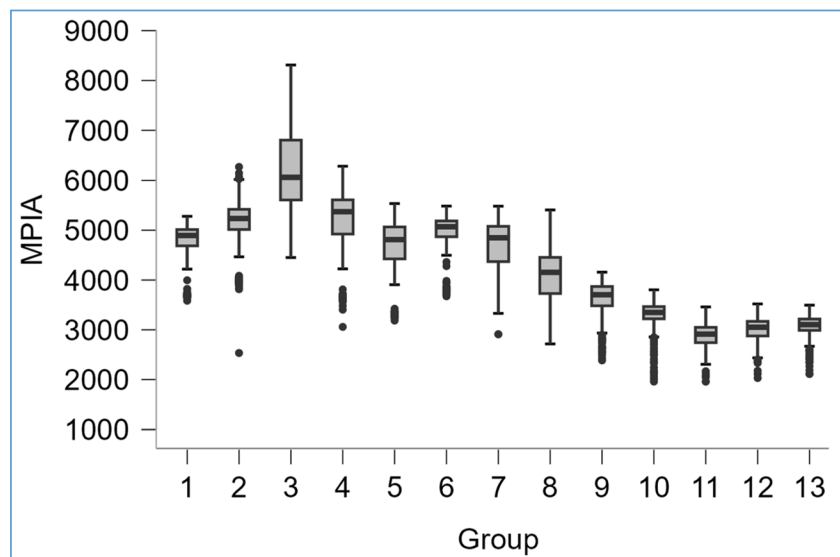
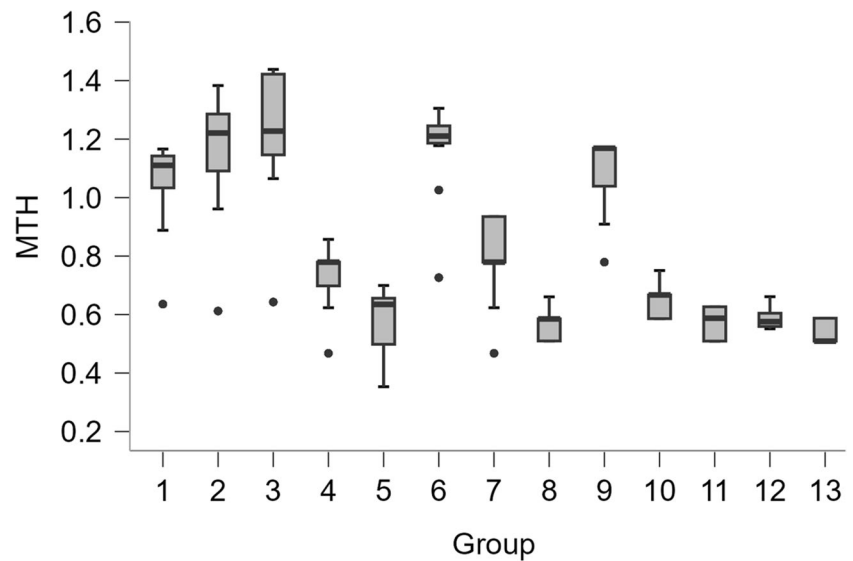


Fig. 11 Box plot of MTH data



2.6 Inferential statistics

Inferential statistics has two components: hypothesis testing and estimation of population characteristics based on a population sample. The hypothesis testing analysis outlines the impact of the independent variables: LSS and SGFR, on the dependent ones: MPT, MPIA, and MTH. At the same time, the populations’ characteristics, MPT, MPIA, and MTH, are inferred based on a sample drawn from the population. Sections 3.6.1, 3.6.2, 3.6.3, and 3.6.4 include the hypothesis testing analysis. Section 4 addresses in detail the estimation of MPA, MPIA, and MTH characteristics based on the data gathered at the monitoring stage.

2.6.1 Experimental design

This research grouped the collected samples based on the LSS and SGFR levels. Three-way ANOVA is the ideal choice to evaluate whether the changes in measured MTH, MPT, and MPIA are significant based on levels of LSS and SGFR. The first factor, LSS, has three levels: (1) low speed (10 mm/s), (2) medium speed (15 mm/s), and high speed (20 mm/s). The second factor, SGFR, has three levels: (1) low flow (9.44 l/min), (2) ideal (medium) flow (18.88 l/min), and (3) high flow (28.32 l/min). The dependent variable, MTH, is physically measured with the microscope, as discussed in Section 3.2.3. Table 8 shows the conducted 3 × 3 factorial design.

2.6.2 Conditions for traditional two-way ANOVA

Before conducting the traditional two-way ANOVA, the ANOVA assumptions [36] for this statistical test are examined, as shown in Table 9. Both conditions of normality

Table 8 The experimental design showing the factor levels in each group

Factor B:	Factor A: SGFR			
	Low SGFR (9.44 l/min)	Ideal SGFR (18.88 l/min)	High SGFR (28.32 l/min)	
LSS				
Slow LSS (10 mm/s)	Slow LSS (10 mm/s) and low flow (9.44 l/min) μ11	Slow LSS (10 mm/s) and ideal flow (18.88 l/min) μ12	Slow LSS (10 mm/s) and high flow (28.32 l/min) μ13	μLSS1
Ideal LSS (15 mm/s)	Ideal LSS (15 mm/s) and low flow (9.44 l/min) μ11	Ideal LSS (15 mm/s) and ideal flow (18.88 l/min) μ12	Ideal LSS (15 mm/s) and high flow (28.32 l/min) μ13	μLSS2
Fast LSS (20 mm/s)	Fast LSS (20 mm/s) and low flow (9.44 l/min) μ21	Fast LSS (20 mm/s) and ideal flow (18.88 l/min) μ22	Fast LSS (20 mm/s) and high flow (28.32 l/min) μ23	μLSS3
	μSGFR1	μSGFR2	μSGFR3	

(evaluated by the Shapiro-Wilks test and summarized in Table 7) and homogeneity of variance (evaluated by Levene’s test and summarized in Table 7) are violated. Therefore, the nonparametric Scheirer-Ray-Hare test (Scheirer, Ray, and Hare [37]) is conducted instead of traditional two-way ANOVA. Then, Dunn’s post hoc test [38] was also conducted to identify the different groups. Figure 12 summarizes the approach followed in the conduction of the statistical testing.

Table 9 Assumptions of traditional ANOVA checked for the experiment data

Assumption	Question	Status
Assumption # 1:	Are factors categorical with two or more groups?	✓
Assumption # 2:	Is the dependent variable continuous?	✓
Assumption # 3:	Are all samples independent?	✓
Assumption # 4:	Is the dependent variable normally distributed for each group of the independent variables?	X
Assumption # 5:	Are outliers cleared?	✓
Assumption # 6:	Is there homogeneity of variances?	X

✓, satisfied; X, unsatisfied

2.6.3 Scheirer-Ray-Hare test

The Scheirer-Ray-Hare test is the nonparametric version of two-way ANOVA. It is used when the data under study fails to meet the assumptions of normality and homogeneity of variance [40] required by the two-way ANOVA analysis. The Scheirer-Ray-Hare test requires that all treatment groups have an equal number of replicates and that the number of replicates is at least 5 [40]. The significance of the main effects, as well as the interactions, is determined by comparing two H -values that approximately follow a χ^2 distribution. Those H -statistics (usually called ϵH – values”) calculated with Scheirer-Ray-Hare’s formula based on the ranks of observation values, and $H_{critical}$ obtained from the χ^2 distribution table [41] are based on the degree of freedom and significance level [40]. The null hypotheses are shown in Table 10 and are summarized as follows:

Fig. 12 Decision tree for selecting the proper hypothesis-testing procedures, adapted from the article by Xie et al. [39]. The path in blue shows the conducted aggregate analysis

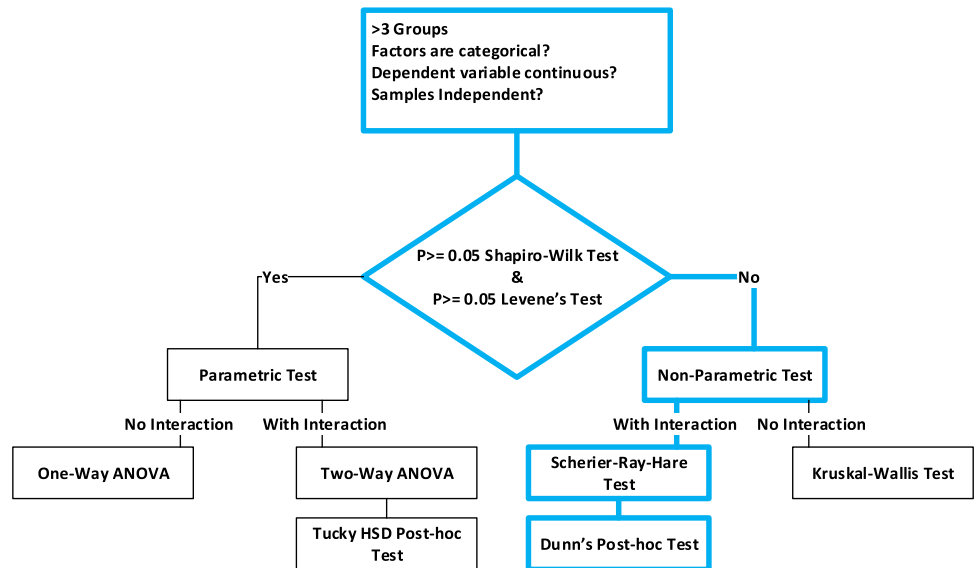


Table 10 The null and alternative hypotheses of the nonparametric Scheirer-Ray-Hare test

Factor A (main effect of LSS):

Null hypothesis:

$$H_{0A} : \mu_{R_{LSS1}} = \mu_{R_{LSS2}} = \mu_{R_{LSS3}}$$

Alternative hypothesis:

H_{1A} : At least one of the means listed in H_{0A} is different from the others

$\mu_{R_{LSSi}}$: meanrankbasedonLSSleveli

Factor B (main effect of SGFR):

Null hypothesis:

$$H_{0B} : \mu_{R_{SGFR1}} = \mu_{R_{SGFR2}} = \mu_{R_{SGFR3}}$$

Alternative hypothesis:

H_{1B} : At least one of the means listed in H_{0B} is different from the others

$\mu_{R_{SGFRi}}$: meanrankbasedonSGFRlevelj

Factor A × factor B (interaction between LSS and SGFR)

Null hypothesis:

$H_{0(AB)}$: Therearenointeractioneffects.

Alternative Hypothesis:

$H_{1(AB)}$: $H_{0(AB)}$ isnottrue

1. The LSS has no effect on the dependent variable (MTH, MPT, or MPIA).
2. The SGFR has no effect on the dependent variable (MTH, MPT, or MPIA).
3. There is no interaction between the effects of LSS and SGFR.

Tables 11, 12, and 13 show the Scheirer-Ray-Hare test results for MTH, MPIA, and MPT, respectively. In each table, the ranks for all the input data elements are obtained. A two-factor ANOVA is then conducted in Microsoft Excel by using the ranks as input. The $H - values$ are calculated by dividing the corresponding sum of squares (SS) value by MS_{Total} . The Scheirer-Ray-Hare test obtains the significance of each factor and the interaction from each respective $H - statistic$ with the respective degree of freedom (df) value listed in Tables 11, 12, and 13 since all the $p-values$ assume values are less than 0.05. Based on the data

collected, it has been determined that there is adequate evidence to support a 95% confidence level regarding the significant impact of SGFR, LSS, and their interaction on MTH, MPIA, and MPT. The LSS has been previously investigated and is found to have a significant effect on the single-track laser cladding geometry [42] and is found to influence both the bonding quality and coating geometry [43]. The SGFR is also investigated for single-track geometry and is also found significant in some cases, as reported by J. Sun et al. [44]. As outlined in Tables 3 and 4, many studies investigate the influence of LSS on MTH and MPT. It is noticeable that previous studies that investigate laser geometry characterization do not include nonparametric statistical investigation that is usually dictated by a lack of normality and homogeneity of variance, as explained in Section 3.5.2.

To satisfy the two-way ANOVA conditions of normality and homogeneity of variance, the treatments for each

Table 11 Scheirer-Ray-Hare test table for MTH based on two-factor SGFR and LSS and their interactions

A: Scheirer-Ray-Hare test (MTH)				Alpha	0.05	
Source of variation	Sum of squares (SS)	Degree of freedom df	Mean square (MS)	$H = \frac{SS}{MS_{total}}$	p-value	sig
SGFR	7.96×10^6	2		30.75	<0.001	Yes
LSS	3.35×10^8	2		1293.15	<0.001	Yes
SGFR × LSS	5.98×10^6	4		23.12	<0.001	Yes
Residual	1.08×10^8	1755				
Total	4.56×10^8	1763	258,845			

Table 12 Scheirer-Ray-Hare test table for MPIA based on two-factor SGFR and LSS and their interactions

B: Scheirer-Ray-Hare test (MPIA)				Alpha	0.05	
Source of variation	Sum of squares (SS)	Degree of freedom df	Mean square (MS)	$H = \frac{SS}{MS_{total}}$	p-value	sig
SGFR	2.76×10^8	2		1062.03	<0.001	Yes
LSS	4.99×10^7	2		192.14	<0.001	Yes
SGFR × LSS	3.85×10^6	4		14.85	<0.001	Yes
Residual	1.28×10^8	1755				
Total	4.57×10^8	1763	259,454.8	4.57×10^8		

Table 13 Scheirer-Ray-Hare test table for MPT based on two-factor SGFR and LSS and their interactions

C: Scheirer-Ray-Hare test (MPT)				Alpha	0.05	
Source of variation	Sum of squares (SS)	Degree of freedom df	Mean square (MS)	$H = \frac{SS}{MS_{total}}$	p-value	sig
SGFR	3.54×10^8	2		1362.59	<0.001	yes
LSS	5.88×10^6	2		22.64	<0.001	yes
SGFR × LSS	2.09×10^7	4		80.37	<0.001	yes
Residual	7.72×10^7	1755				
Total	4.57×10^8	1763	2.59×10^5	4.57×10^8		

factor should be set so that they are not drastically different. This ensures, in turn, that the dependent variables are not as drastically different either. However, this study covers a relatively large range of parameter treatments: 15–20 mm/s LSS and 9.4–28.3 l/min. This approach enriches the collected observations by covering a wider range of parameters, which match the factor screening and characterization [36] nature of such a study.

2.6.4 Post-hoc test (Dunn's test)

After conducting the Scheirer-Hare-Ray test, if the null hypothesis is rejected, indicating significant effects of certain factors or interactions on the dependent variable, it becomes essential to compare the individual groups to determine which groups differ from each other. Dunn's multiple comparison test is conducted, as shown in Fig. 12, by applying pairwise comparisons to determine which groups differ significantly from one another. A 95% confidence interval is used to determine which groups are significantly different. The null hypothesis for Dunn's test indicates no statistical difference noted between the studied groups. In contrast, the alternate hypothesis for Dunn's test states that there is a significant difference between the different groups.

Table 14 shows the pairwise comparisons between the MTH, MPIA, and MPT data groups conducted with JASP [33]. Most comparisons show that the difference is significant (p -value < 0.05). MTH comparisons show that group 6: (SGFR = 28.26 l/min \times LSS = 20 m/s) and group 9: (SGFR = 9.42 l/min \times LSS = 20 m/s) are not significantly different. Another comparison shows an insignificant difference is observed between MPIA data between group 1 (SGFR = 18.84 l/min \times LSS = 15 m/s) and group 3 (SGFR = 18.84 l/min \times LSS = 20 m/s). A detailed discussion of the results of the different tests carried out is presented in Section 4.

3 Results and discussion

This section discusses the results of the various conducted statistical tests presented in Section 3 and provides an in-depth interpretation of them based on the physics of the process and the discussed literature in Section 2. It is noticed that different clusters are spread into relatively large ranges of MP, MPIA, and MTH. These large ranges are driven due to the various melt pool interactions that would not be realized with an experimental study. A simple mean (or median in case of non-parametric statistical analysis) would not reveal the actual effect of parameters on the MP, MPIA, and MTH. So, instead of handling the whole group data, the individual means of the 12 tracks are visualized and compared in Sects. 4.1 to 4.7. Sections 4.1–4.3 summarize and discuss

the influence of LSS on MPT, MPIA, and MTH, respectively, and Sects. 4.4–4.6 articulate the effects of SGFR on MTP, MPIA, and MTH, respectively. Section 4.7 dominates the selection and application of the heat zones that are driven by LP and LSS. Finally, Section 4.8 describes the significance of the findings.

3.1 Influence of LSS on MPT under different levels of SGFR

Figure 13 shows three subplots. Each subplot includes three graphs of average MPT versus track numbers measured with different levels of LSS. Each subplot belongs to a different level of SGFR. The LSS levels are a low level of 10 mm/s, a medium level of 15 mm/s, and a high level of 20 mm/s. The levels of SGFR are a low level of 9.4 l/min, a medium level of 18.88 l/min, and a high level of 28.32 l/min.

The figure includes six defined cases: In cases 1, 3, and 5, which represent the MPT at the first track, the MPT decreases as the LSS increases; in case 2, which represents the MPT of tracks 2 to 12, the MPT increases as the LSS increases from 10 to 15 mm/s and from 15 to 20 mm/s; in case 4, which represents the MPT of tracks 4 to 12, has two opposite trends. The MPT increases as the LSS increases from 10 to 15 mm/s, and the MPT decreases as the LSS increases from 15 to 20 mm/s. In case 6, which represents the MPT of tracks 4 to 12, the MPT decreases as LSS increases. In addition, the figure includes three heat range zones: feasible cladding, overheating, and insufficient heating zones. The cladding zone in which the MPT falls between 1650 and 1850 °C is categorized as the feasible cladding zone. The cladding zone in which the MPT reaches levels above 1850 °C is categorized as an overheating zone. The cladding zone in which the MPT reaches levels below 1650 °C is categorized as an insufficient heating zone. These heat zones can help understand the behavior of MTH and MPIA in Sects. 4.2 and 4.3. A description of the selection and demonstration of the effect of heat zones is outlined in Section 7.7.

In cases 1, 3, and 5, the reduction of MPT with increasing the LSS, which is very small, is an expected result as the low LSS includes exposing the melt pool to more laser power (laser energy), in which the cladding takes place on the first tracks, on the flat substrate. The opposite trend observed in cases 2 and 4, under low and medium SGFR, in which MPT increases slightly with increasing the LSS, can be explained as the functional coating samples with a slower LSS produce tracks with more powder deposition and MTH than those with a higher LSS. This extra deposition makes the slopes of the tracks steeper [45]. As a result, the inclined surface increases the area exposed to the laser beam and reduces the energy absorption [28], resulting in relatively lower MPT. On the other hand, a

Table 14 Dunn’s post-hoc multiple comparison test for all groups

Pairwise Comparison								MTH Rank	MPIA Rank	MPT Rank
First group				Second group				p-value	p-value	p-value
Group	SGFR l/min	LSS mm/s	LP Watt	Group	SGFR l/min	LSS mm/s	LP Watt			
G2	9.44	10	1575	G4	9.44	15	1575	< .001*	0.962	< .001*
G2	9.44	10	1575	G5	9.44	20	1575	< .001*	< .001*	< .001*
G2	9.44	10	1575	G6	18.88	10	1575	0.32	0.002*	< .001*
G2	9.44	10	1575	G7	18.88	15	1575	< .001*	< .001*	0.007*
G2	9.44	10	1575	G8	18.88	20	1575	< .001*	< .001*	< .001*
G2	9.44	10	1575	G9	28.32	10	1575	0.013*	< .001*	< .001*
G2	9.44	10	1575	G10	28.32	15	1575	< .001*	< .001*	< .001*
G2	9.44	10	1575	G12	28.32	20	1575	< .001*	< .001*	< .001*
G4	9.44	15	1575	G5	9.44	20	1575	< .001*	< .001*	0.69
G4	9.44	15	1575	G6	18.88	10	1575	< .001*	0.002*	< .001*
G4	9.44	15	1575	G7	18.88	15	1575	0.091	< .001*	< .001*
G4	9.44	15	1575	G8	18.88	20	1575	< .001*	< .001*	< .001*
G4	9.44	15	1575	G9	28.32	10	1575	< .001*	< .001*	< .001*
G4	9.44	15	1575	G10	28.32	15	1575	< .001*	< .001*	< .001*
G4	9.44	15	1575	G12	28.32	20	1575	< .001*	< .001*	< .001*
G5	9.44	20	1575	G6	18.88	10	1575	< .001*	0.001*	< .001*
G5	9.44	20	1575	G7	18.88	15	1575	< .001*	0.994	< .001*
G5	9.44	20	1575	G8	18.88	20	1575	0.012*	< .001*	< .001*
G5	9.44	20	1575	G9	28.32	10	1575	< .001*	< .001*	< .001*
G5	9.44	20	1575	G10	28.32	15	1575	< .001*	< .001*	< .001*
G5	9.44	20	1575	G12	28.32	20	1575	0.086	< .001*	< .001*
G6	18.88	10	1575	G7	18.88	15	1575	< .001*	0.001*	< .001*
G6	18.88	10	1575	G8	18.88	20	1575	< .001*	< .001*	0.553
G6	18.88	10	1575	G9	28.32	10	1575	< .001*	< .001*	< .001*
G6	18.88	10	1575	G10	28.32	15	1575	< .001*	< .001*	< .001*
G6	18.88	10	1575	G12	28.32	20	1575	< .001*	< .001*	< .001*
G7	18.88	15	1575	G8	18.88	20	1575	< .001*	< .001*	0.002*
G7	18.88	15	1575	G9	28.32	10	1575	< .001*	< .001*	< .001*
G7	18.88	15	1575	G10	28.32	15	1575	< .001*	< .001*	< .001*
G7	18.88	15	1575	G12	28.32	20	1575	< .001*	< .001*	< .001*
G8	18.88	20	1575	G9	28.32	10	1575	< .001*	< .001*	< .001*
G8	18.88	20	1575	G10	28.32	15	1575	< .001*	< .001*	< .001*
G8	18.88	20	1575	G12	28.32	20	1575	0.428*	< .001*	< .001*
G9	28.32	10	1575	G10	28.32	15	1575	< .001*	< .001*	0.006*
G9	28.32	10	1575	G12	28.32	20	1575	< .001*	< .001*	< .001*
G10	28.32	15	1575	G12	28.32	20	1575	< .001*	0.001*	< .001*

“*” indicates that the difference is significant, and results in red color refer are insignificant (i.e., p -value < 0.05)

unique trend, in which the MPT decreases by less than 50 °C as the LSS increases from 15 to 20 mm/s under medium SGFR for the overlapping tracks, the inclined surface which increases the area exposed to the laser beam

[28], but also there high powder flow due to the interaction SGFR and CGFR (see Section 4.6) the powder is deflected forward and sideways out of the laser-material interaction

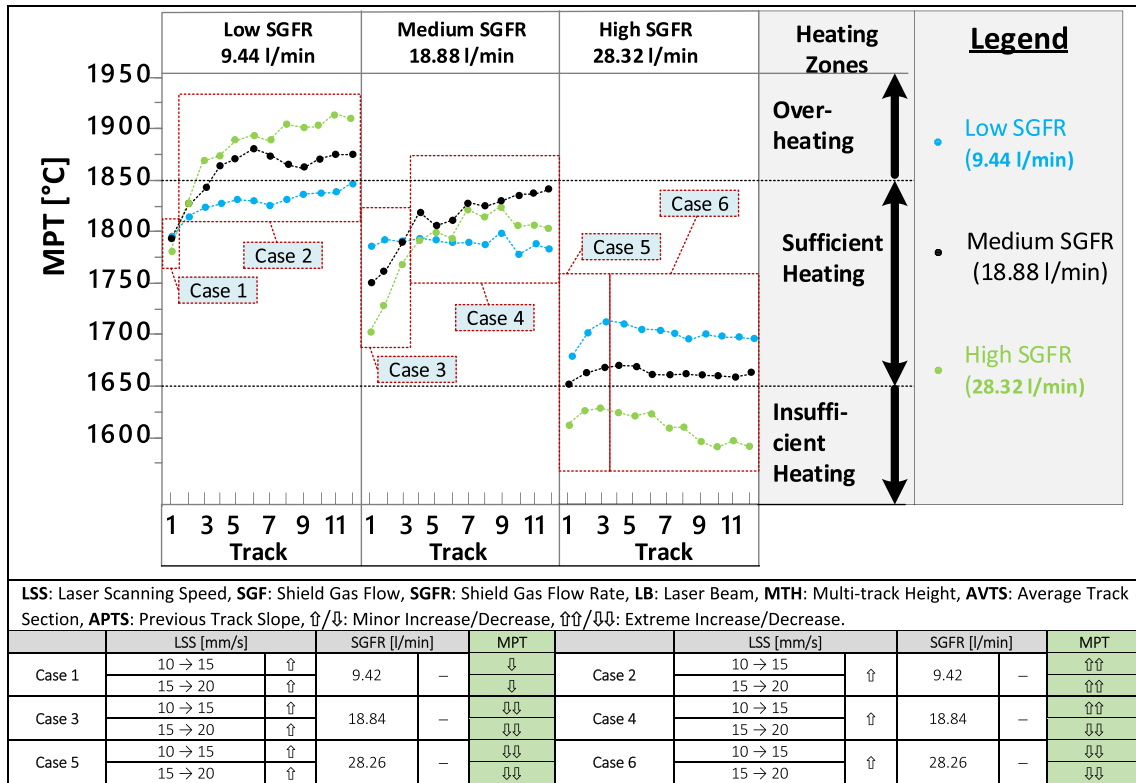


Fig. 13 Simple main effect plot showing the effect of LSS on MPT

due to the slope of the previous tracks, leaving less powder under the laser beam. So, this increases the MPT.

Unlike the increase in MPT with increasing the LSS observed in cases 3 and 5 with the overlapping tracks, case 6 shows a slight decrease in MPT with increasing the LSS under high SGFR. The cooling effect [5] from the SGFR, which naturally increases with increasing SGFR value, can explain this slight reduction of MPT when increasing the LSS in case 3 since the SGFR is at its highest level.

Notably, the cladding within the overheating zone and the one within the insufficient heating zones is of poor quality due to the risk of cladding, porosity, and lack of fusion, respectively.

3.2 Influence of LSS on MPIA under different levels of SGFR

Figure 14 shows three subplots. Each subplot includes three graphs of average MPIA versus track numbers measured with different levels of LSS. Each subplot belongs to a different level of SGFR. The LSS levels are a low level of 10 mm/s, a medium level of 15 mm/s, and a high level of 20 mm/s. The levels of SGFR are a low level of 9.4 l/min, a medium level of 18.88 l/min, and a high level of 28.32 l/min.

The figure includes three defined cases. In those three cases (cases 1, 2, and 3), which represent the MPIA along

the range of cladding from track 1 to 12, the MPIA increases as the LSS decreases regardless of the level of SGFR.

MPIA represents the area of the melt pool obtained by a coaxial camera. MPIA is a projection area of the melt pool which is deposited on the flat substrate in the case of the first track, and a projection area of the melt pool, which is deposited partly on the sloped track shoulder and partly on the flat substrate in the case of subsequent overlapping tracks. In the two cases (first track, subsequent overlapping tracks), the projection area is linked to the amount of powder deposited. Accordingly, the MPIA increases as LSS decreases regardless of the level of SGFR.

3.3 Influence of LSS on MTH under different levels of SGFR

Similar to the previous two figures, Fig. 15 shows three subplots. Each subplot includes three graphs of average MTH vs. track numbers measured with different levels of LSS. Each subplot belongs to a different level of SGFR. The LSS levels are a low level of 10 mm/s, a medium level of 15 mm/s, and a high level of 20 mm/s. The levels of SGFR are a low level of 9.4 l/min, a medium level of 18.88 l/min, and a high level of 28.32 l/min.

The figure includes three defined cases. In those three cases (cases 1, 2, and 3), which represent the MTH along the

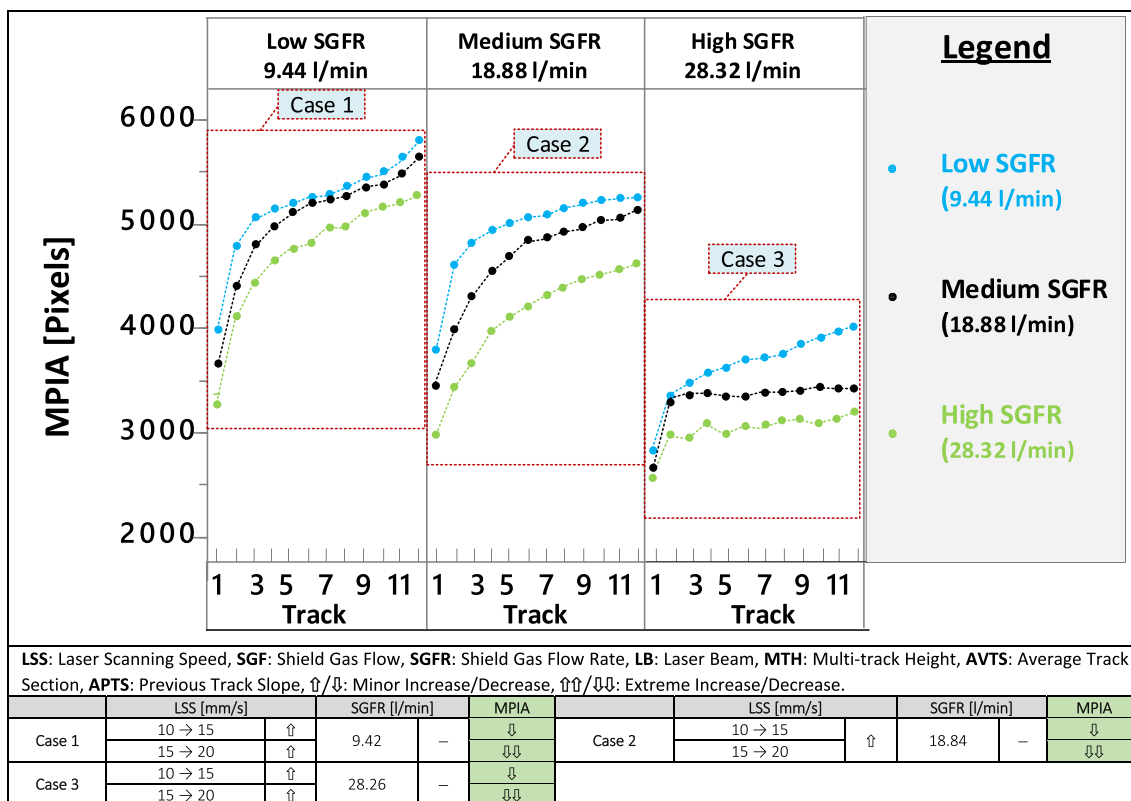


Fig. 14 Simple main effect plot of LSS on MPIA

range of cladding from track 1 to 12, the MTH increases as the LSS decreases, regardless of the level of SGFR.

The leading cause for this MTH increase is attributed to more powder deposited when reducing the LSS. The powder catchment efficacy [45] and the interaction time become less when the LSS increases, causing the height to decrease. It is also worth mentioning that the cladding within the overheating zone (Fig. 13) and the one within the insufficient heating zones are of poor quality due to the risk of cladding, porosity, and lack of fusion, respectively. So, the results of such cases cannot be generalized unless the parameters (LP, LSS, SGFR) are the same.

3.4 Influence of SGFR on MPT under different levels of LSS

Figure 16 shows three subplots. Each subplot includes three graphs of average MPT versus track numbers measured with different levels of SGFR. Each subplot belongs to a different level of LSS. The LSS levels are a low level of 10 mm/s, a medium level of 15 mm/s, and a high level of 20 mm/s. The levels of SGFR are a low level of 9.4 l/min, a medium level of 18.88 l/min, and a high level of 28.32 l/min. In addition, the figure includes three heat range zones: feasible cladding, overheating, and insufficient heating zones. The cladding

zone in which the MPT falls between 1650 and 1850 °C is categorized as the feasible cladding zone. The cladding zone in which the MPT reaches levels above 1850 °C is categorized as an overheating zone. The cladding zone in which the MPT reaches levels below 1650 °C is categorized as an insufficient heating zone. These heat zones can help understand the behavior of MTH and MPIA in Sects. 4.5 and 4.6. A description of the selection and demonstration of the effect of heat zones is outlined in Section 7.7.

The figure includes three defined cases. In those three cases (cases 1, 2, and 3), which represent the MPT along the range of cladding from track 1 to 12, the MPT decreases as the SGFR increases. This reduction of MPT with increasing the SGFR occurs due to the cooling effect associated with increasing the SGFR [5]. The significantly low MPT observed in the graph of high LSS (20 mm/s) and high SGFR (28.32) of case 3 indicates a high risk for lack of fusion. The lack of fusion is further studied in, section 3.7.

3.5 Influence of SGFR on MPIA under different levels of LSS

Figure 17 shows three subplots. Each subplot includes three graphs of average MPIA versus track numbers measured with different levels of SGFR. Each subplot belongs to a

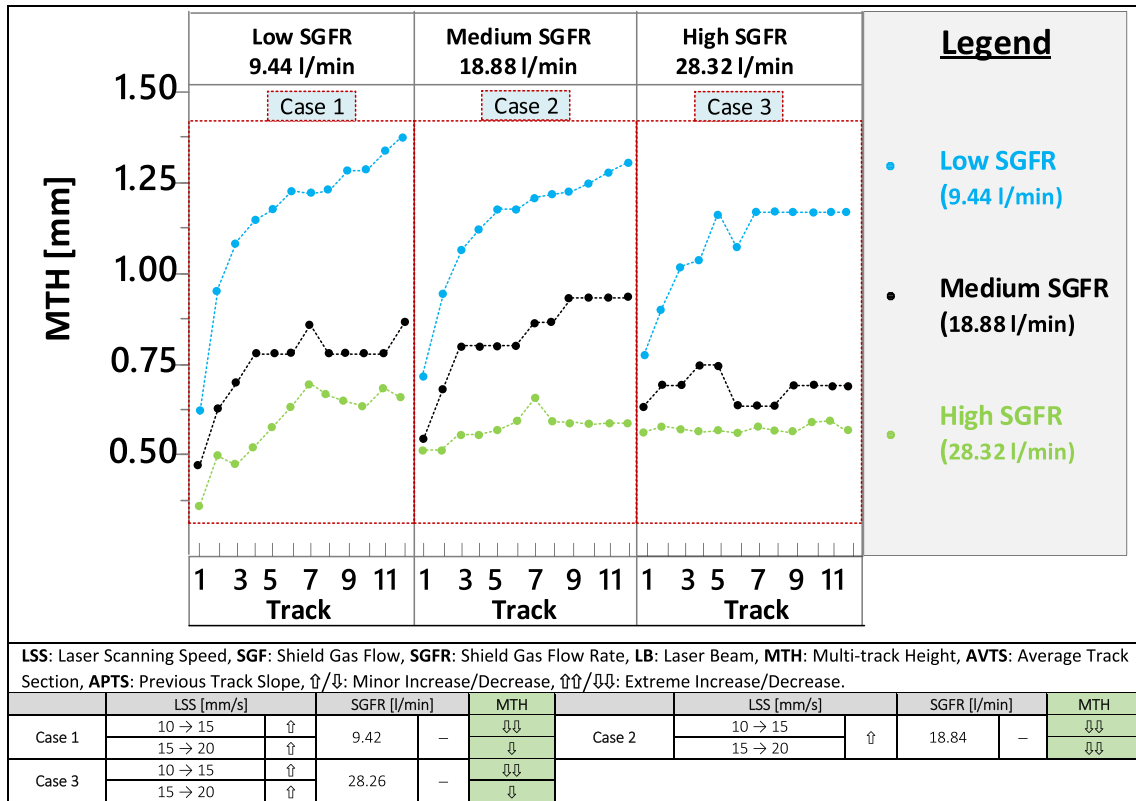


Fig. 15 Simple main effect plot of LSS on MTH

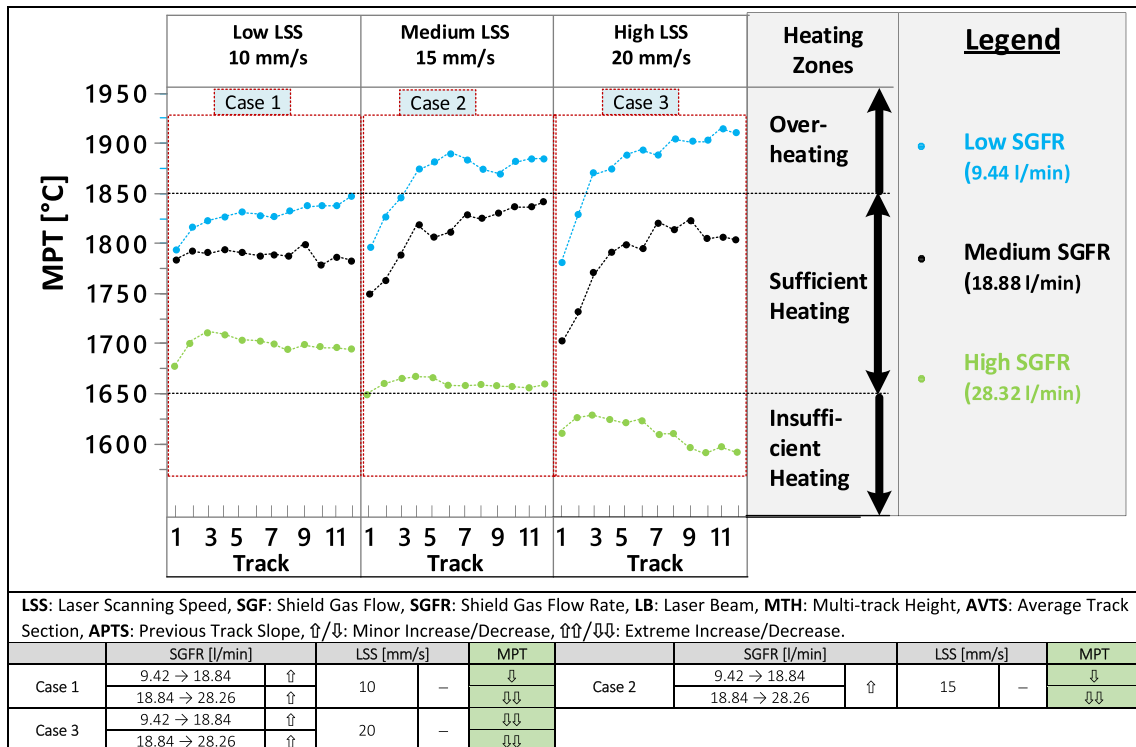


Fig. 16 Simple main effect plot of SGFR on MPT

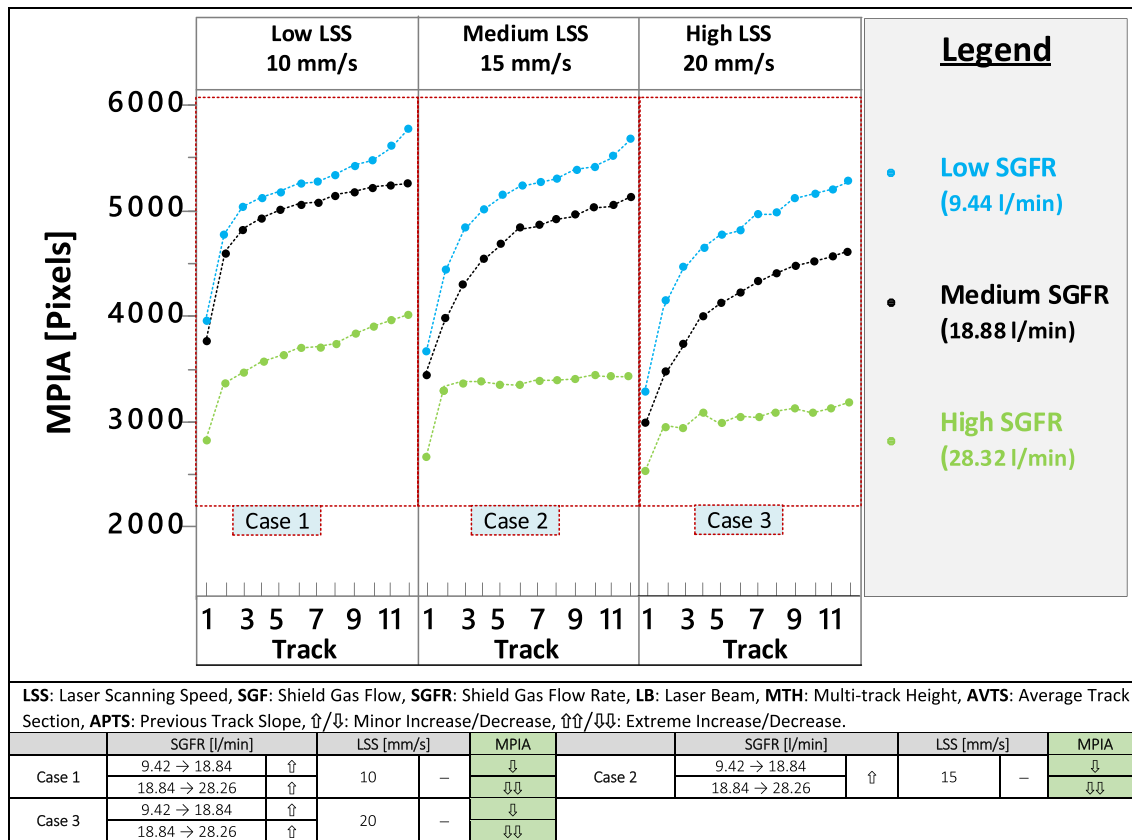


Fig. 17 Simple main effect plot of SGFR on MPIA

different level of LSS. The LSS levels are a low level of 10 mm/s, a medium level of 15 mm/s, and a high level of 20 mm/s. The levels of SGFR are a low level of 9.4 l/min, a medium level of 18.88 l/min, and a high level of 28.32 l/min.

The figure includes three defined cases. In those three cases (cases 1, 2, and 3), which represent the MPIA along the range of cladding from track 1 to 12, the MPIA decreases as the SGFR increases. This reduction in MPIA is associated with the turbulence that increases with the increase in SGFR. This turbulence promotes the blowing away [5] of the powder around the melt pool (excess powder) before joining the melt pool bath. It is worth mentioning that the effect of the turbulence is more apparent at the high level of SGFR.

3.6 Influence of SGFR on MTH under different levels of LSS

Figure 18 shows three subplots. Each subplot includes three graphs of average MTH versus track numbers measured with different levels of SGFR. Each subplot belongs to a different level of LSS. The LSS levels are a low level of 10 mm/s, a medium level of 15 mm/s, and a high level of 20 mm/s. The levels of SGFR are a low level of 9.4 l/min, a medium level of 18.88 l/min, and a high level of 28.32 l/min.

The figure includes six defined cases: Cases 1, 3, and 5 represent the average MTH at the first track, first two tracks, and first four tracks, respectively. In the three cases (cases 1, 3, and 5) the MTH increases as the SGFR increases; in cases 2 and 6, which represent the MTH of tracks 2 to 12 and 5 to 12, the MTH increases as the SGFR decreases; in case 4, which represents the MTH of tracks 3 to 12, has two opposite trends: the MTH increases as the SGFR increase from 9.4 to 18.88 l/min, while The MTH decreases as the SGFR increase from 18.88 to 28.32 l/min.

In cases 1, 3, and 5, the increase of the height with the increase of SGFR in the first track is attributed to a reduction in the oxidation kinetics as the SGFR increases. The oxidation kinetics increase by increasing the MPT (Eo et al. 2020). The MPT is inversely correlated to the increase of the SGFR. Even though the turbulence, which increases by increasing the SGFR, might cause the powder to be blown away, the effect of the turbulence seems not dominant in the first track of case 1, the two first tracks of case 3, and the first 4 tracks of case 5.

The reduction in oxidation kinetics with the increase of SGFR is dominant in the first track of cases 1, 3, and 5. However, this reduction in oxidation kinetics which still affects the MTH in some tracks after the first track (case

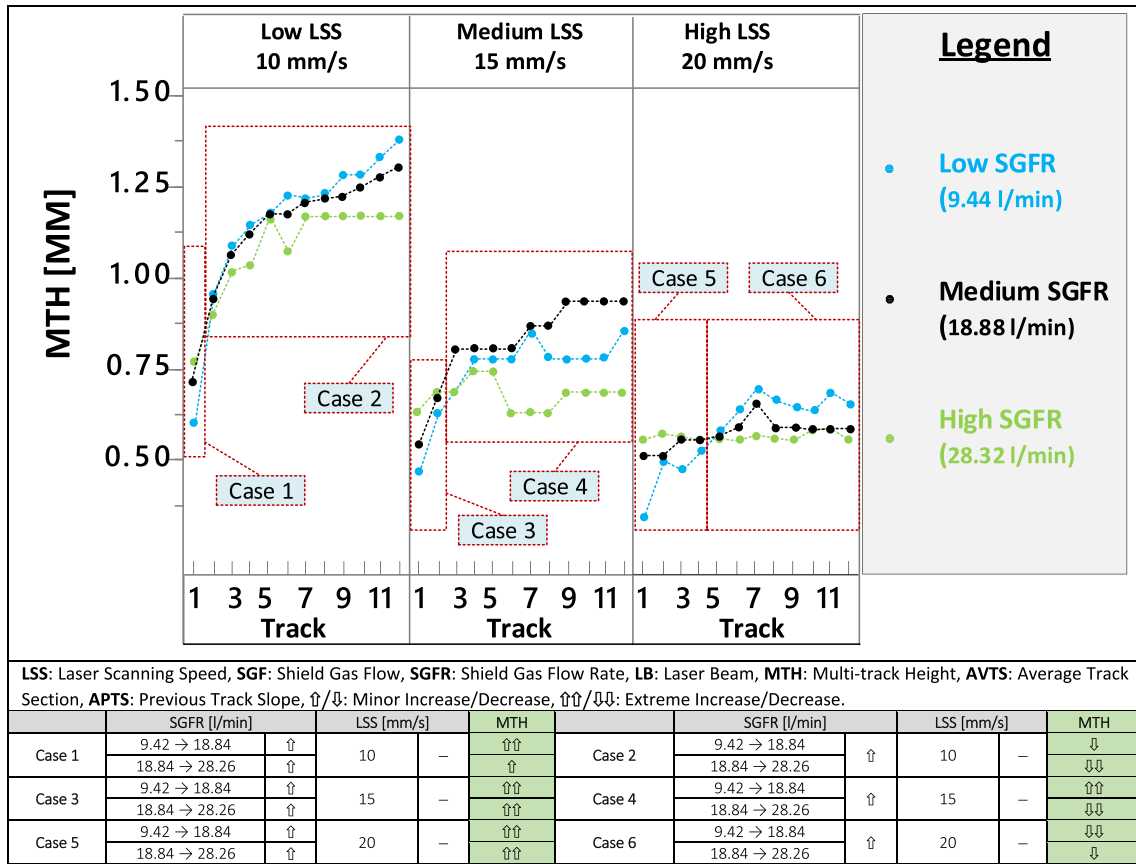


Fig. 18 Simple main effect plot of SGFR on MTH

3 tack 2, and case 5 tracks 2,3 and 4) becomes gradually less dominant while the turbulence effect that increases with SGFR increase becomes gradually more dominant and as more tracks are built leading to cases 4, 2, and 6. Increasing the turbulence with increasing the SGFR causes the powder to be blown away [5]. In their study, Koti et al. [45] conclude that when overlapping tracks are added to previous tracks, the gas and particles are deflected forward and sideways out of the laser-material interaction zone. It is also worth mentioning that the cladding within the overheating zone (Fig. 16) and the one within the insufficient heating zones are of poor quality due to the risk of cladding, porosity, and lack of fusion, respectively. So, the results of such cases cannot be generalized unless the parameters (LP, LSS, SGFR) are the same.

3.7 Effect of process parameters on heating of the melt pool and quality of coatings

In some of the cases of MPT discussed in Sects. 3.1 and 3.4, extremely low and high MPTs can indicate cases of insufficient heating and overheating, respectively. This section studies the effect of LP combined with LSS and SGFR on

MPT and MT, focusing on overheating and insufficient heating. Improper selection of LP and LSS can lead to overheating and lack of fusion defects. Overheating resulting from excessive LP, slow LSS, or both causes relatively lengthy exposure to the laser beam and thus results in excessive heat input. Conversely, insufficient LP, high LSS, or both cause a lack of fusion due to relatively brief exposure to the laser beam, yielding a lack of heat input for proper fusion. Overheating is not desired as it causes cracks and bubbles in the functional coating. On the other hand, insufficient heating reduces the strength of the functional coating and leads to defects such as a lack of fusion [29]. Figure 19 shows the plots for average MPT (Fig. 19i), MPIA (Fig. 19ii), and MTH (Fig. 19iii). In each plot, there are three subplots. Each subplot includes two graphs of data measured under two combinations of LSS and SGFR: a first combination of low LSS (10 mm/s and low SGFR (9.44 l/min; and a second combination of high LSS (20 mm/s and high SGFR (28.32 l/min. Each subplot belongs to a different level of LP. The LP levels are a low level of 1425 W, a medium level of 1575 W, and a high level of 1725 W. In addition, Fig. 19i includes three temperature range zones: feasible cladding, overheating, and insufficient heating zones. Even though

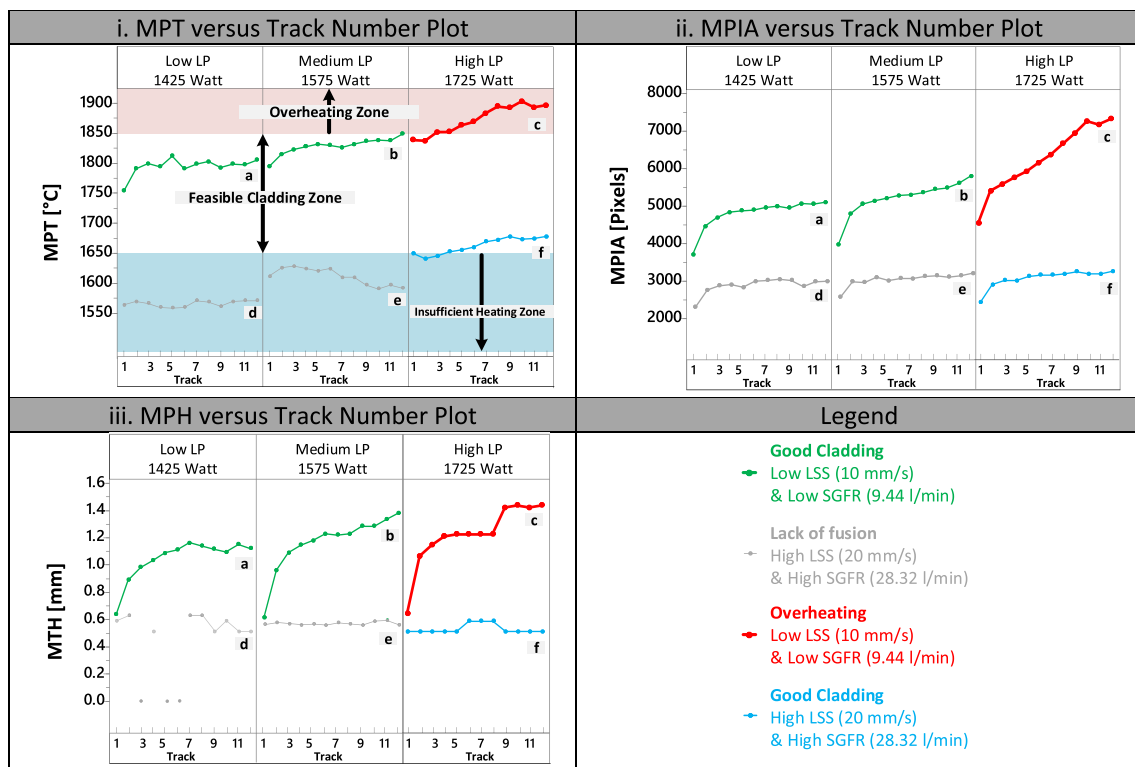


Fig. 19 Effect of LP combined with LSS and SGFR on MPT, MPIA, and MTH. Process parameters for graphs a, b, and c: low LSS (10 mm/s) and low SGFR (9.44 l/min). Process parameters for graphs d, e, and f: high LSS (20 mm/s) and high SGFR (28.32 l/min)

the cold rolled structural steel substrate's melting point is around 1370 °C, and the 316 L HIS powder material's melt point is between 1375 and 1400 °C), the physical quality inspection of the samples obtained in this study and those samples of related studies reveals that the range of good (feasible) cladding is obtained at MPT between 1650 and 1850 °C. This study, though, unlike most of the literature that tackles single beads, addresses multi-track coatings. This threshold applies to the 316 L HIS powder material cladding on cold rolled structural steel substrate, irrespective of the various processing conditions used. The cladding zone in which the MPT reaches levels above 1850 °C is categorized as an overheating zone. The cladding zone in which the MPT reaches levels below 1650 °C is categorized as an insufficient heating zone. Obtained results demonstrate that changes in the values of both LSS and LP should be coordinated in a manner to maintain the adequate heating of the melt pool and thus arrive at healthy specimens. LSS of 10 mm/s along with low-to-medium LP levels, as well as LSS of 20 mm/s along with high LP, produce plausible specimens. Otherwise, underheating is recorded at a high-level LSS of 20 mm/s at both low and medium LP levels, while overheating is recorded at a low-level LSS of 10 mm/s and a high LP level.

In the MPT versus track number plot, graphs a, b, and f represent adequately heated clads, as they fall within the feasible cladding zone; graph c represents overheated clads; and graphs d and e represent insufficiently heated clads. In the MPIA versus track number plot, graphs a, b, and f, which exhibit adequately heated cladding seams, represent the same samples in graphs a, b, and f in the MPT versus track number plot. Graph c, which represents overheated clads, shows a rapid increase in MPIA as the LP level increases from 1575 to 1725 W; and graphs d and e, which represent insufficiently heated clads, do not show a significant effect of LP on MPIA as the LP level increases from 1425 to 1575 W.

In the MTH versus track number plot, graphs a, b, and f, which exhibit good cladding seam, represent the same samples in graphs a, b, and f (except for track 1) in the MPT versus track number; graph c, which represents overheated clads, shows a sudden increase in MTH on track 9; graph e, which represent insufficiently heated clads, also shows lack of fusion (see Fig. 20); graph d, which represents again insufficiently heated clads, shows a major lack of fusion (see Fig. 21). In case of overheating, there is a risk of entrapping bubbles, over-melting, and crack formation. Cracks and entrapped bubbles can explain the sudden change in MTH and insufficient heating.

Fig. 20 Lack of fusion for the sample shown in Fig. 19iii chart e (left). A magnified image lacks fusion at track 11 (right)

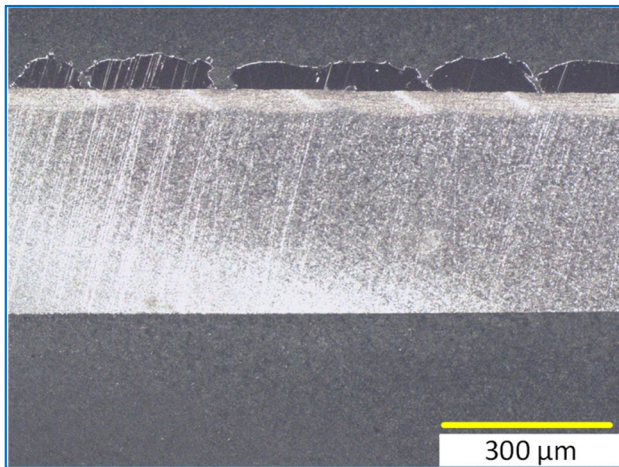
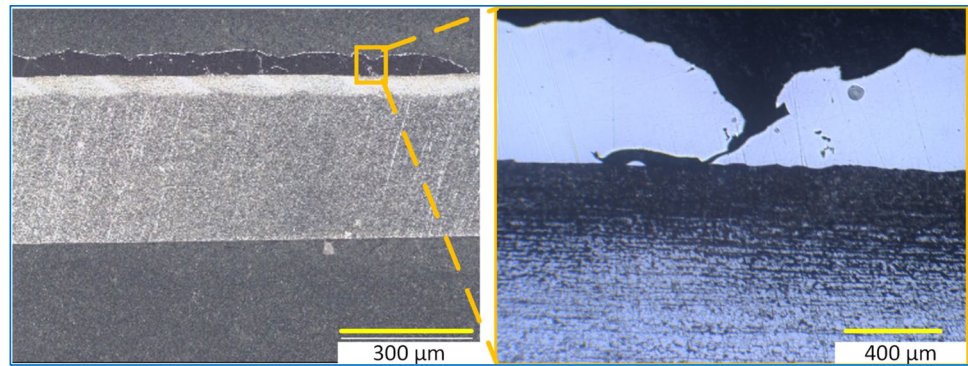


Fig. 21 Lack of fusion for the sample shown in Fig. 19iii chart d

4 Summary of discussion

Sections 4.1–4.6 summarize the main relationships between LSS and SGFR at one end and MPT, MPIA, and MTH at the other. The LSS and SGFR have shown a significant influence on the MTH, MPIA, and MPT, which nominates LSS and SGFR to be predictors in future ML models that can be used to predict the MTH, MTP, and MPIA. It has been noted that there is a need to include additional independent variables to help explain the broad variability of MTP, MIA, and MTH, particularly because of the complex nature of the melt pool interaction. This becomes essential when the MPT falls within overheating or an insufficient heating zone. Within those overheating and insufficient heating zones, there is a risk of cracking, porosity, and lack of fusion. Thus, selecting parameters that yield operating outside the feasible cladding zones could enhance the knowledge further about quality defects in laser cladding. On the other hand, this study

characterizes the MPIA for the first time in the literature, using monitored data of multi-track clads, which opens the door for more studies that help improve the body of knowledge on LAM-DED possibly contributing to cost savings by finding optimized process parameters. For example, our findings indicate that good quality cladding resulting in the largest MTH is obtained with 15 mm/s LSS and 18.84 l/min SGFR. A separate experiment has also been conducted to examine the combined effect of both LSS and LP on the quality of the specimens. Results demonstrate that changes in the values of both factors should be coordinated in order to upkeep the adequate heating of the melt pool and thus arrive at healthy specimens. Otherwise, defective ones are produced, exhibiting a lack of fusion and low strength of the coating when underheated, or specimens with cracks and bubbles when overheated.

5 Conclusion and future work

This study aims to characterize the influence of LSS and SGFR on MPT, MPIA, and MTH for functional-coating laser cladding. The study is carried out on a five-axis CNC equipped with a diode laser cladding head and a powder feeder with a continuous coaxial nozzle. The powder used is 316 L HIS with particle size between 53 and 150 μm . The substrate is cold-rolled structural steel. A 3×3 multi-level full factorial design is conducted, in which LSS has two levels, and SGFR has three levels. The nonparametric alternative for two-way ANOVA, the Sheirer-Ray-Hare test, is utilized because of the lack of normality and homogeneity of variance in MPT, MPIA, and MTH data. The study successfully established the statistical relationship between LSS and SGFR on the one hand and MTH, MPIA, and MPT on the other. It shows that the individual factors, LSS and SGFR, and their interactions significantly affect the MTH, MPIA, and MPT. This investigation contributes to the knowledge

addressing functional coatings using LAM-DED, especially in cases when SGFR is involved as a process parameter. The potential poor quality for samples that fall with overheating and insufficient heating is also addressed in this study, providing more explanation for MTH and MPIA reaction to the process parameters. The coordination needed between the LSS and LP process parameters is established in production of healthy specimens.

The simple main effect of the utilized process parameters in this study, LSS, and SGFR, on the process signatures and response (part quality metric), MPT, MPIA, and MTH of the multi-track functional coating, is discussed. The results have been analyzed in light of the previous findings and insights from past studies. It is found that the effect of LSS and SGFR on the MTH at the first track is different from that on the following tracks. It is believed that such findings will motivate the study of laser cladding of multi-track functional coating; the literature, as pointed out, tends to rely on findings of laser cladding of single track. Obtaining optimized coatings with maximal resulting MTH will drive cost savings.

As far as the limitations of this study are concerned, it has to be stated that such provided characterization will accurately depict such a LAM-DED performed on the given setup and the given process parameters: laser power, powder flow rate, laser spot size, and laser powder size. Thus, additional studies are required to extrapolate and generalize the results of the analysis conducted in this research, given a broader range of parameters within and outside the operation window of laser cladding.

Future work shall address the relationships between the process signatures: MPT and MPIA at one end and the part quality metrics such as MTH at another. A noticeable trend is spotted in the conducted study that calls for further investigation. It is believed that the time-series analysis of the multi-track coating should be studied and how that relates to the possible production of faulty specimens beyond a certain track number and vice versa. The results of this research can be utilized further when creating process models utilizing in-situ monitoring to optimize the process parameters. On the other hand, the variability within some groups under the same LSS and SGFR conditions leads us to believe that more features are necessary to obtain robust ML models. The methodology employed in the current characterization and variability analysis can be extended to characterize the mechanical properties of multi-track functional coatings, such as microhardness and porosity. Geometric features sensitive to SGFR (e.g., steps and pockets) where there is a sudden change in geometry can be investigated for design for additive manufacturing.

Lastly, the conducted variability analysis and characterization strengthen the authors' belief that LSS and LP are essential features in future machine learning models to be constructed in our future work for predicting MTH as ML would be used to predict part quality metrics, equipment failures, and support parameter selection to enhance the flexibility and agility of the LAM-DED process. Future studies will also allow mapping MTH against both process parameters and signatures and encourage consideration of other quality metrics and other mechanical and physical characteristics of functional coating.

Author contribution M. Mousa, with the aid of H. Osman and A. Azab, has conducted the study conception, design, and methodology. M. Mousa and A. El-Gaddar have contributed to the sample preparation and data collection and have carried out the statistical analysis with directions provided by H. Osman. M. Mousa, H. Osman, and A. Azab have contributed to the analysis and interpretation of results. M. Mousa, H. Osman, and A. Azab have contributed to the manuscript and rebuttal preparation. F. Baki and A. Azab have supervised this project and have provided the funding.

Acknowledgments The authors are indebted to all the efforts and support provided by Lincoln Laser Solutions for all the support provided to conduct the experiments made at their facilities in Oldcastle, Ontario. This research project has been funded by an internal Faculty of Engineering, University of Windsor Industry Engineering Partnership Catalyst Grant, and an NSERC Discovery Grant RGPIN-2017 06897.

Declarations

Conflict of interest The authors declare no competing interests.

References

1. Fayaz, Gholamreza, and Sepideh S Zakeri. 2021. "Laser cladding of metals by additive manufacturing: moving toward 3D printing." In *Laser Cladding of Metals*, 33–57 Springer
2. Vandone A, Valente A (2022) AI based monitoring system for DED part quality evaluation. *Procedia CIRP* 107:635–640. <https://doi.org/10.1016/j.procir.2022.05.038>
3. Bernhard, Neef, Wiche, Wesling, Hoff, Hermsdorf, and Kaierle. 2021. "Bernhard 2021 importance of shield gas." In *Laser Cladding of Metals*, 1–7. © Springer Nature Switzerland AG
4. Ye J, Bab-hadiashar A, Alam N, Cole I (2023) A review of the parameter-signature-quality correlations through in situ sensing in laser metal additive manufacturing. *Int J Adv Manuf Technol* 124(5–6):1401–1427. <https://doi.org/10.1007/s00170-022-10618-0>
5. Koruba P, Wall K, Reiner J (2018) Influence of processing gases in laser cladding based on simulation analysis and experimental tests. *Procedia CIRP* 74:719–723. <https://doi.org/10.1016/j.procir.2018.08.025>
6. Nasiri S, Khosravani MR (2021) Machine learning in predicting mechanical behavior of additively manufactured parts. *J Market Res* 14:1137–1153

7. Singh Ambrish, Kapil Sajan, Das Manas (2020) A comprehensive review of the methods and mechanisms for powder feedstock handling in directed energy deposition. *Addit Manuf* 35:101388. <https://doi.org/10.1016/j.addma.2020.101388>
8. Liu H, Qin X, Huang S, Zeqi Hu, Ni M (2018) Geometry modeling of single track cladding deposited by high power diode laser with rectangular beam spot. *Opt Lasers Eng* 100:38–46. <https://doi.org/10.1016/j.optlaseng.2017.07.008>
9. Spears TG, Gold S (2016) In-process sensing in selective laser melting (SLM) additive manufacturing. *Integr Mater Manuf Innov* 5(1):16–40. <https://doi.org/10.1186/s40192-016-0045-4>
10. Haley, James, Jaydeep Karandikar, Callan Herberger, Eric MacDonald, Thomas Feldhausen, and Yousub Lee. 2024. "Review of in situ process monitoring for metal hybrid directed energy deposition." *J Manuf Process Elsevier Ltd*. <https://doi.org/10.1016/j.jmapro.2023.12.004>
11. You D, Gao X, Katayama S (2013) Multiple-optics sensing of high-brightness disk laser welding process. *NDT E Int* 60:32–39. <https://doi.org/10.1016/j.ndteint.2013.07.005>
12. Hofman JT, Pathiraj B, Van Dijk J, De Lange DF, Meijer J (2012) A camera based feedback control strategy for the laser cladding process. *J Mater Process Technol* 212(11):2455–2462. <https://doi.org/10.1016/j.jmatprotec.2012.06.027>
13. Gibson BT, Bandari YK, Richardson BS, Henry WC, Vetland EJ, Sundermann TW, Love LJ (2020) Melt pool size control through multiple closed-loop modalities in laser-wire directed energy deposition of Ti-6Al-4V. *Addit Manuf* 32:100993. <https://doi.org/10.1016/j.addma.2019.100993>
14. Ahn D-G (2021) Directed energy deposition (DED) process: state of the art. *Int J Precis Eng Manuf Green Technol* 8(2):703–742. <https://doi.org/10.1007/s40684-020-00302-7>
15. Yuan Junlin, Liu Hanru, Liu Weiwei, Wang Fengtao, Peng Shitong (2022) A method for melt pool state monitoring in laser-based direct energy deposition based on DenseNet. *Measurement* 195:111146. <https://doi.org/10.1016/j.measurement.2022.111146>
16. Xi W, Song B, Zhao Y, Yu T, Wang J (2019) Geometry and Dilution Rate Analysis and Prediction of Laser Cladding. *Int J Adv Manuf Technol* 103 (9–12):4695–4702. <https://doi.org/10.1007/s00170-019-03932-7>
17. Sampson R, Lancaster R, Sutcliffe M, Carswell D, Hauser C, Barras J (2021) The influence of key process parameters on melt pool geometry in direct energy deposition additive manufacturing systems. *Opt Laser Technol* 134:106609. <https://doi.org/10.1016/j.optlastec.2020.106609>
18. Farshidianfar MH, Khajepour A, Gerlich AP (2016) Effect of real-time cooling rate on microstructure in laser additive manufacturing. *J Mater Process Technol* 231:468–478. <https://doi.org/10.1016/j.jmatprotec.2016.01.017>
19. Figueredo EWA, Apolinario LHR, Santos MV, Silva ACS, Avila JA, Lima MSF, Santos TFA et al (2021) Influence of laser beam power and scanning speed on the macrostructural characteristics of AISI 316L and AISI 431 stainless steel depositions produced by laser cladding process. *J Mater Eng Perform* 30(5):3298–3312. <https://doi.org/10.1007/s11665-021-05676-6>
20. Raj, Dhiraj, Saikat R. Maity, and Bipul Das. 2022. State-of-the-art review on laser cladding process as an in-situ repair technique. *Proceedings of the Institution of Mechanical Engineers, Part E: Journal of Process Mechanical Engineering*. Vol. 236. SAGE Publications Ltd. <https://doi.org/10.1177/09544089211044558>
21. Sommer Niklas, Stredak Florian, Böhm Stefan (2021) High-speed laser cladding on thin-sheet-substrates—influence of process parameters on clad geometry and dilution. *Coatings* 11(8):952. <https://doi.org/10.3390/coatings11080952>
22. Kattire P, Paul S, Singh R, Yan W (2015) Experimental characterization of laser cladding of CPM 9V on H13 tool steel for die repair applications. *J Manuf Process* 20:492–499. <https://doi.org/10.1016/j.jmapro.2015.06.018>
23. (2020) Controlling inclusion evolution behavior by adjusting flow rate of shielding gas during direct energy deposition of AISI 316 L. *Addit Manuf* 33:101119. <https://doi.org/10.1016/j.addma.2020.101119>
24. Kummilil J, Sammarco C, Skinner D, Brown CA, Rong K (2005) Effect of Select LENS™ processing parameters on the deposition of Ti-6Al-4V. *J Manuf Process* 7(1):42–50. [https://doi.org/10.1016/S1526-6125\(05\)70080-3](https://doi.org/10.1016/S1526-6125(05)70080-3)
25. Arthur, N, K Malabi, P Baloyi, H Moller, & S Pityana, and Narthur@csir Co Za. 2016. "Influence of process parameters on layer build-up and microstructure of Ti6Al4V (ELI) alloy on the optomec lens."
26. Srisungsitthisunti P, Kaewprachum B, Yang Z, Gao G (2022) Real-time quality monitoring of laser cladding process on rail steel by an infrared camera. *Metals* 12(5):825. <https://doi.org/10.3390/met12050825>
27. Hua T, Jing C, Xin L, Fengying Z, Weidong H (2008) Research on molten pool temperature in the process of laser rapid forming. *J Mater Process Technol* 198(1–3):454–462. <https://doi.org/10.1016/j.jmatprotec.2007.06.090>
28. Kledwig Christian, Perfahl Holger, Reisacher Martin, Brückner Frank, Bliedner Jens, Leyens Christoph (2019) Analysis of melt pool characteristics and process parameters using a coaxial monitoring system during directed energy deposition in additive manufacturing. *Materials* 12(2):308. <https://doi.org/10.3390/ma120308>
29. Zheng Y, Liu F, Gao J, Liu F, Huang C, Zheng H, Wang P, Qiu H (2023) Effect of different heat input on the microstructure and mechanical properties of laser cladding repaired 300M steel. *J Market Res* 22:556–568. <https://doi.org/10.1016/j.jmrt.2022.11.153>
30. Hao Ce, Liu Z, Xie H, Zhao K, Liu S (2020) Real-time measurement method of melt pool temperature in the directed energy deposition process. *Appl Therm Eng* 177:115475
31. Ocelík V, Eekma M, Hemmati I, De Hosson JThM (2012) Elimination of Start/Stop Defects in Laser Cladding. *Surf Coat Technol* 206(8–9):2403–249. <https://doi.org/10.1016/j.surfcoat.2011.10.040>
32. Thiruvikraman, P K. 2019. "The image processing toolbox." In *A Course on Digital Image Processing with MATLAB®*. <https://doi.org/10.1088/978-0-7503-2604-9ch10>
33. JASP Team. 2022. "JASP (Version 0.16.3)[Computer Software]." JASP - Free and User-Friendly Statistical Software
34. Shapiro SS, Wilk MB (1965) An analysis of variance test for normality (complete samples). *Biometrika* 52(3–4):591–611. <https://doi.org/10.1093/biomet/52.3-4.591>
35. Levene, H. 1960. "Levene test for equality of variances." *Contributions to Probability and Statistics*, 278–92
36. Montgomery, Douglas C. 2017. "Montgomery: design and analysis of experiments." John Willy & Sons
37. Scheirer CJ, Ray W, Hare N (1976) The analysis of ranked data derived from completely randomized factorial designs. *Biometrics* 32(2):429–34
38. Dunn OJ (1964) Multiple comparisons using rank sums. *Technometrics* 6(3):241. <https://doi.org/10.2307/1266041>

39. Xie Y, Wang H, Chen Y, Liu F, Yao M, Zhang L, Liu P, Hong Q, Chi X, Dongchuan Yu (2022) Establishing normative data for the number cancellation test among children in kindergartens and primary schools in China. *Front Psych* 13:1–9. <https://doi.org/10.3389/fpsyg.2022.788825>
40. Sokal RR, Rohlf FJ (1995) *Biometry: the principles and practice of statistics in biological research*, 3rd edn. W.H Freeman and Company, New York, NY, USA
41. Zar JH (2010) *Biostatistical Analysis* 5th, 5th edn. Practice Hall, New Jersey
42. Sun Yuwen, Hao Mingzhong (2012) Statistical analysis and optimization of process parameters in Ti6Al4V laser cladding using Nd:YAG laser. *Opt Lasers Eng* 50(7):985. <https://doi.org/10.1016/j.optlaseng.2012.01.018>
43. Bourahima F, Helbert AL, Rege M, Ji V, Solas D, Baudin T (2019) Laser cladding of Ni based powder on a Cu-Ni-Al glassmold: influence of the process parameters on bonding quality and coating geometry. *J Alloy Compd*. <https://doi.org/10.1016/j.jallcom.2018.09.004>
44. Sun J, Zhao Yu, Yang L, Zhao X, Wanrui Qu, Tianbiao Yu (2019) Effect of shielding gas flow rate on cladding quality of direct laser fabrication AISI 316L stainless steel. *J Manuf Process* 48:51–65. <https://doi.org/10.1016/j.jmapro.2019.10.011>
45. Koti D, Powell J, Naesstroem H, Voisey KT (2023) Powder catchment efficiency in laser cladding (directed energy deposition). An investigation into standard laser cladding and the ABA cladding technique. *J Laser Appl* 35(1):012025. <https://doi.org/10.2351/7.0000904>

Publisher's Note Springer Nature remains neutral with regard to jurisdictional claims in published maps and institutional affiliations.

Springer Nature or its licensor (e.g. a society or other partner) holds exclusive rights to this article under a publishing agreement with the author(s) or other rightsholder(s); author self-archiving of the accepted manuscript version of this article is solely governed by the terms of such publishing agreement and applicable law.